Universal Control in 1e-2n Spin System Utilizing Anisotropic Hyperfine Interactions

by

Yingjie Zhang

A thesis
presented to the University of Waterloo
in fulfillment of the
thesis requirement for the degree of
Master of Science
in
Physics

Waterloo, Ontario, Canada, 2010

I hereby declare that I am the sole author of this thesis. This is a true copy of the thesis, including any required final revisions, as accepted by my examiners.

I understand that my thesis may be made electronically available to the public.

Abstract

ESR quantum computing presents faster means to perform gates on nuclear spins than the traditional NMR methods. This means ESR is a test-bed that can potentially be useful in ways that are not possible with NMR. The first step is to demonstrate universal control in the ESR system. This work focuses on spin systems with one electron spin and two nuclear spins. We try to demonstrate control over the nuclear spins using the electron as an actuator.

In order to perform the experiments, a customized ESR spectrometer was built in the lab. The main advantage of the home-built system is the ability to send arbitrary pulses to the spins. This ability is the key to perform high fidelity controls on the spin system.

A customized low temperature probe was designed and built to have three features necessary for the experiments. First, it is possible to orient the sample, thus to change the spin Hamiltonian of the system, in situ. Second, the combined system is able to perform ESR experiments at liquid nitrogen and liquid helium temperatures and rotate the sample while it is cold. Last, the pulse bandwidth of the microwave resonator, which directly affects the fidelity of the gates, is held constant with respect to the sample temperature.

Simulations of the experiments have been carried out and the results are promising. Preliminary experiments have been performed, the final set of experiments, demonstrating full quantum control of a three-spin system, are underway at present.

Acknowledgments

First of all, I must thank Dr. Jonathan Baugh for supervising me. During the course of my masters program, Dr. Baugh taught me numerous lessons that one can ever hope for. His working ethic also sets an example for me. I am more than honored to have the opportunity to be able to work with Dr. Baugh. I want to thanks the rest of my committee members, Dr. Raymond Laflamme and Dr. Thorsten Hesjedal, for guiding me through my study and giving me suggestions when I needed.

I also want to thank all the post-docs and students who helped me and worked with me. In particular, I want to thank Dr. Colm Ryan, for spending much time with me teaching me how to be an experimentalist, helping me understand the underlying physics of ESR, Dr. Bill Coish for his clear explanations in theoretical physics, Jeremy Chamilliard for helping me figure out the spectrometer, sharing his insights on experiments and Jen Fung, James Mracek and Yipu Song for sharing their knowledge on quantum dots.

The science machine shop at the university of Waterloo is the main factor behind our home-built low temperature probe. Harmen Vander Heide gave me invaluable suggestions on designing the probe, Michael Lang's specialty in machining made the probe available and Hiruy Haile made the student shop such a pleasant place to work in.

I would also like to thank Mike Chong in Chemistry for the usefully discussions on sample preparation, as well as Jalil Assound for X-ray irradiation.

My work would not be possible without the hospitality of IQC and its members. I want to thank everyone at IQC for making my stay like home.

Last but not the least, I want to thank my parents Qiuju Ma and Wenqing Zhang, to whom, I own everything. I want to thank their undying support and continuous trust in me. They are my motivation behind this. This thesis is for them.

Dedication

This is dedicated to my parents.

Contents

List of Tables

List of Figures

Chapter 1

Introduction

1.1 Quantum computation

Quantum computers in principle can solve many classically intractable problems[16]. The most famous example is factoring large numbers[20]. The power of quantum computers come from properties only available to quantum particles, such as superposition and entanglement. Similar to classical computers, which use bits as fundamental information units, quantum computers use quantum bits (or qubits). The difference between classical bits and qubits is that classical bits have to be either 0 or 1 while qubits can be 0, 1 or an arbitrary superposition of 0 and 1. For quantum computers, well-defined qubits are required[5]. Some choices of qubits include spins, photons and special superconducting circuits.

Spin-1/2 particles can be used as qubits because they have two well-defined states, spin-up and spin-down. The spin is in superposition when it is not aligned in the up-down axis. Some spin-1/2 particles such as an electron, proton and carbon-13 nucleus have been used as qubits for certain physical implementations of quantum computing. This work reported here focuses on electron spin resonance (ESR) techniques used to control a system containing these three types of spins.

1.2 Fundamentals of ESR and ESR quantum computing

The concept of ESR is very similar to nuclear magnetic resonance (NMR). The spin-1/2 electron exhibit energy difference (i.e. Zeeman energy) in the two spin state (up and down)

while placed in a magnetic field. The energy difference E between the two states is governed by:

$$E = h\nu = g\mu_B B_0 \tag{1.1}$$

where h is Planck's constant, ν is the resonance frequency (or Larmor frequency) that describes the energy difference between the two states, g is the g-factor of the electron, μ_B is Bohr magneton and B_0 is the static magnetic field.

When a microwave pulse with a frequency ν is applied, the electron spin rotates a certain angle based on the total energy of the pulse. By varying the power and the length of the pulse, single-qubit gates such as NOT (which flips the electron spin) can be implemented.

In this work we only focus on ensemble systems, meaning samples that contain many copies of the same molecule of interest. Each molecule is one quantum processor, and the end-result measured is the average of all results from each molecule. This is an expectation value measurement.

The motivation of doing quantum computing with ESR comes from NMR quantum computing. In NMR, nuclear spins are used as qubits and radio frequency pulses are used to perform operations on the qubits. NMR has been an ideal test-bed for quantum computing[7] and several important algorithms have been demonstrated by NMR[12][3]. ESR is very similar to NMR. The qubits in ESR systems are electron spins (and nuclear spins depending on the system). Due to electron's intrinsic higher gyromagnetic ratio than nuclei, the controls are normally microwave pulses. In this thesis, spin systems with one unpaired electron and one/two nearby nuclear spin(s) are considered.

The main advantages of using ESR compared with NMR is that $\sim 10^3$ times faster quantum gates can be implemented in ESR. The Zeeman energy is $\sim 10^3$ times larger in ESR than in NMR. In NMR, a single qubit gate normally takes microseconds. On the other hand, it (typically) only requires nanoseconds to perform single-qubit gates in ESR. In addition, due to relatively weak dipole-dipole interactions between the nuclei ($\sim$KHz), two-qubit gates in NMR take milliseconds to perform. However, in ESR, the electron couples to its surrounding nuclei though hyperfine interactions that are much ($\sim 10^3$ times) stronger than the direct dipole-dipole interactions between nuclei. Therefore, utilizing hyperfine interaction makes it possible to control the nuclear spins much faster than the traditional NMR methods. More detail is described in next section. Another advantage of ESR is that at the same sample temperature, electron spins have $\sim 10^3$ times larger spin polarization due to its larger gyromagnetic ratio. The calculations are shown in appendix A.

There are also disadvantages to using ESR. The electron spins typically have shorter spin-lattice (T_1) and spin-spin (T_2) relaxation times. Detailed explanations of T_1 and T_2 can be found in chapter 2 of Levitt[13]. It is also more challenging to design systems that have both good bandwidth and good signal level that are both essential for experiments. This is discussed in detail in section 2.2.

1.3 Universal control using anisotropic hyperfine coupling in 1e-1n system

As mentioned previously, it is possible to control the nuclear spins through electron via hyperfine interactions. In order to illustrate this, it is important to examine the spin Hamiltonian. In the most basic one-electron-one-nucleus (1e-1n) system, the spin Hamiltonian $\mathcal{H}_0$ has the form[19] (after secular approximation)

$$\mathcal{H}_0 = \omega_S S_Z + \omega_I I_Z + A S_Z I_Z + B S_Z I_X \tag{1.2}$$

where ω_S is the Larmor frequency for the electron spin, ω_I is the Larmor frequency for the nuclear spin, A is the isotropic hyperfine coupling coefficient, B is the anisotropic hyperfine coefficient, S_X, S_Y and S_Z are the Pauli X, Y and Z operators acting on the electron spin, I_X, I_Y and I_Z are the Pauli X, Y and Z operators acting on the nuclear spin respectively. The spin Hamiltonian can also be written in matrix form as

$$\begin{pmatrix} \frac{\omega_S}{2} + \frac{\omega_I}{2} + \frac{A}{4} & \frac{B}{4} & 0 & 0 \\ \frac{B}{4} & \frac{\omega_S}{2} - \frac{\omega_I}{2} - \frac{A}{4} & 0 & 0 \\ 0 & 0 & -\frac{\omega_S}{2} + \frac{\omega_I}{2} - \frac{A}{4} & -\frac{B}{4} \\ 0 & 0 & -\frac{B}{4} & -\frac{\omega_S}{2} - \frac{\omega_I}{2} + \frac{A}{4} \end{pmatrix} \tag{1.3}$$

After diagonalizing the matrix, the eigenstates for the system are

$$|1\rangle = \cos(\frac{\eta_\alpha}{2}) |\alpha\alpha\rangle - \sin(\frac{\eta_\alpha}{2}) |\alpha\beta\rangle \tag{1.4}$$

$$|2\rangle = \sin(\frac{\eta_\alpha}{2}) |\alpha\alpha\rangle + \cos(\frac{\eta_\alpha}{2}) |\alpha\beta\rangle \tag{1.5}$$

$$|3\rangle = \cos(\frac{\eta_\beta}{2}) |\beta\alpha\rangle - \sin(\frac{\eta_\beta}{2}) |\beta\beta\rangle \tag{1.6}$$

$$|4\rangle = \sin(\frac{\eta_\beta}{2}) |\beta\alpha\rangle + \cos(\frac{\eta_\beta}{2}) |\beta\beta\rangle \tag{1.7}$$

where $\eta_\alpha = arctan(\frac{-B}{A+2\omega_I})$, $\eta_\beta = arctan(\frac{-B}{A-2\omega_I})$, $|\alpha\beta>$ indicates the electron spin is in $|\alpha>$ or spin-up state, and the nuclear spin in in $|\beta>$ of spin-down state. The transition probability between each state is calculated by

$$p = |\psi_a>^\dagger S^- |\psi_b> \tag{1.8}$$

where $|\psi_a>$ and $|\psi_b>$ are the two eigenstates of interest, S^- is the lowering operator, $S^- = S_X - iS_Y$. With different choices of A and B, the probabilities of transitions can be varied. When all transitions are accessible, and with the ability to drive one transition (with bandwidth covering all transitions), universal control is possible in the system. In

order to control the system efficiently, meaning that gates have high fidelity and are as short as possible, proper choices of the hyperfine coefficients A and B should be made so that all transitions have relatively large probabilities.

The control in ESR is to drive one or several available electron transition(s). The mathematical form of the control can be described as

$$\mathcal{H}_{con} = \omega_1(t)(\cos\theta S_X + \sin\theta S_Y) \tag{1.9}$$

where ω_1 is the strength of the microwave magnetic field and is time-dependent, θ is the phase. Due to the complex free evolution of the spin Hamiltonian, gradient ascent pulse engineering (GRAPE)[8] is used to design high-fidelity gates. Hodges et al.[11] have demonstrated controlled-NOT (electron being the control bit and nucleus being the target bit) using GRAPE with good fidelity experimentally.

1.4 Universal control in 1e-2n system

The goal of this thesis is to show that universal control utilizing anisotropic hyperfine interactions can be achieved in 1e-2n system. The spin Hamiltonian for a 1e-2n spin system can be described as

$$\mathcal{H}_0 = \omega_S S_Z + \omega_{I1} I_{1Z} + A_1 S_Z I_{1Z} + B_1 S_Z I_{1X} + \omega_{I2} I_{2Z} + A_2 S_Z I_{2Z} + B_2 S_Z I_{2X} \tag{1.10}$$

where ω_{I1} and ω_{I2} are the Larmor frequencies of the two nuclei, A and B are isotropic and anisotropic hyperfine coupling coefficients with the subscripts indicating the particular nuclear spin. The dipole-dipole interactions between the two nuclear spins is neglected since its strength is normally more than 100 times smaller than the electron-nuclear hyperfine interactions.

The 3-spin system has eight eigenstates, and the transition probabilities are also governed by equation 1.8. In order to have good control over the entire system, both sets of hyperfine coefficients should be chosen carefully to ensure that all transitions can be accessed relatively easily. Once again, with the use of GRAPE, by only having the ability to drive electron transitions, high-fidelity universal control can be achieved. One example experiment this thesis tries to demonstrate is to perform a controlled-NOT gate on the two nuclear spins with the electron spin acting as an actuator.

1.5 Layout of the thesis

The following of the thesis is divided into four chapters. Chapter 2 talks about the apparatus including the home-built ESR spectrometer, the resonator and the low-temperature

probe, for the experiments. Chapter 3 focuses on the malonic acid sample used in experiments and gives some important characteristics. Chapter 4 depicts procedures to prepare for experiments and simulations of the experiments. Finally, chapter 5 looks at future directions and concludes this thesis.

Chapter 2

Apparatus

2.1 ESR spectrometer

Commercial ESR systems are widely available for studies of radical molecules and electronic defects in solids. The main draw-back of the commercial systems from the viewpoint of quantum information processing is that pulses applied to the spins are only available in simple forms (such as square pulses). In order to demonstrate universal control through the use of GRAPE pulses, which are typically strongly modulated pulses, a customized system is required.

Figure 2.1 shows the schematic of the homebuilt x-band (8-12GHz) ESR spectrometer. The microwave source provides a CW output. The arbitrary waveform generator (AWG) gives the ability to create arbitrary pulse shapes with 1ns timing resolution. The AWG is key for allowing GRAPE and other arbitrarily modulated pulses to be implemented. The IQ modulator is a device that enables inputs to both X and Y control channels, i.e. 0° and 90° phase components (quadrature). Both inputs are generated by the AWG. The 1kW traveling wave tube (TWT) amplifier amplifies the pulses to the power levels required for exciting the spins efficiently. Finally, the control fields are sent through a circulator into the resonator where the sample is placed. The circulator also directs the signal originating from the sample spins to the receiver arm, consisting the switch, which is used to protect the receiver during pulse inputing stage, and then to the receiver, to demodulate the signal and display it on the oscilloscope, then finally transfer to the computer.

There is one operational detail worth mentioning. The IQ modulator does not respond linearly to the input power. In most uses, the IQ modulator receives inputs with different powers for the in-phase and quadrature channels. Ideally, the output of each channel would be proportional to the input power, and the phase of the output would be the same as of the input. Unfortunately, due to the nonlinear response of the IQ modulator, the actual phase

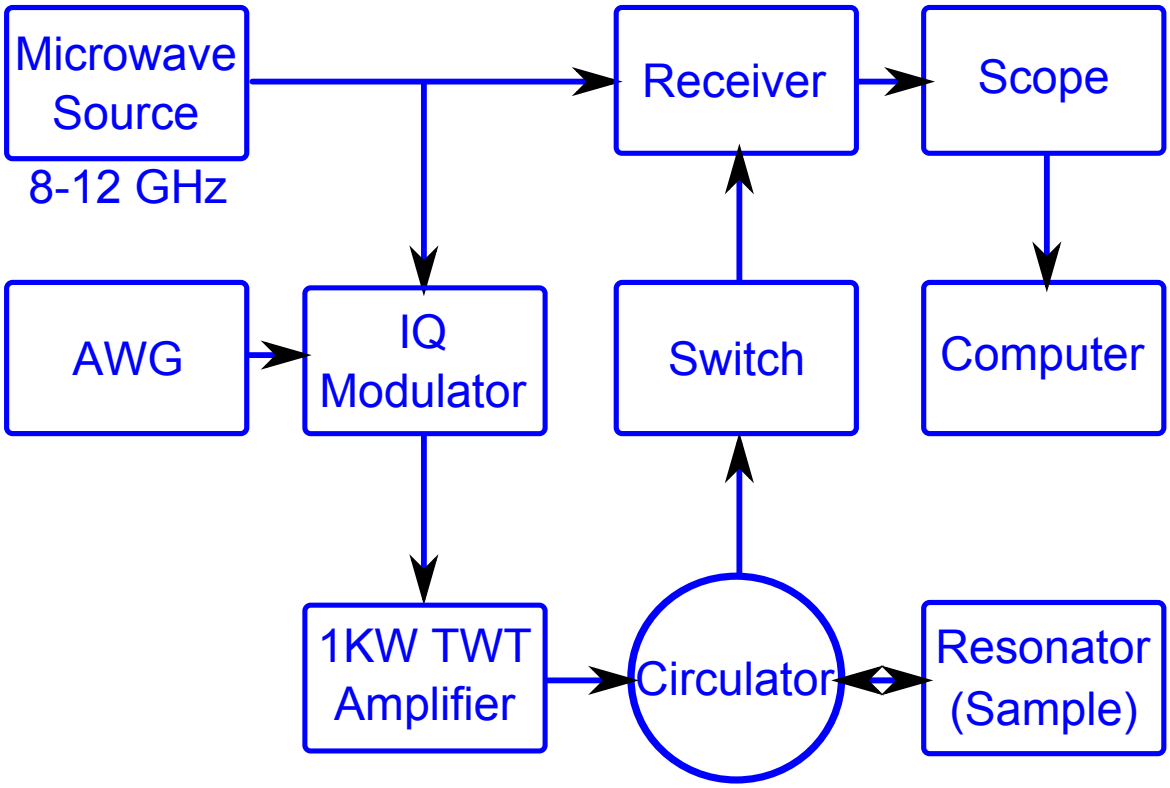

Figure 2.1: Schematic of the homebuilt x-band ESR spectrometer. The microwave source provides carrier frequencies for the input pulses to match the resonance frequency of the resonator. The arbitrary waveform generator (AWG) is used to produce arbitrary input pulse shapes. The IQ modulator enables inputs to both in-phase and quadrature channels. The circulator and the switch are used to make sure the output signal from the sample goes to the receiver while minimal power is reflected back to the TWT amplifier. The demodulated signal is then displayed on the oscilloscope and also recorded on the computer.

based on the outputs would be different from the ideal phase based on the inputs. This error is crucial in quantum information context and should be minimized. The solution to this problem is to use IQ modulator as a single side-band mixer. The two inputs to the IQ modulator now have the same amplitude (which ensures the output and input phases are the same), none-zero frequency and differ by a $\pi/2$ phase. The detail is illustrated in Figure 2.2.

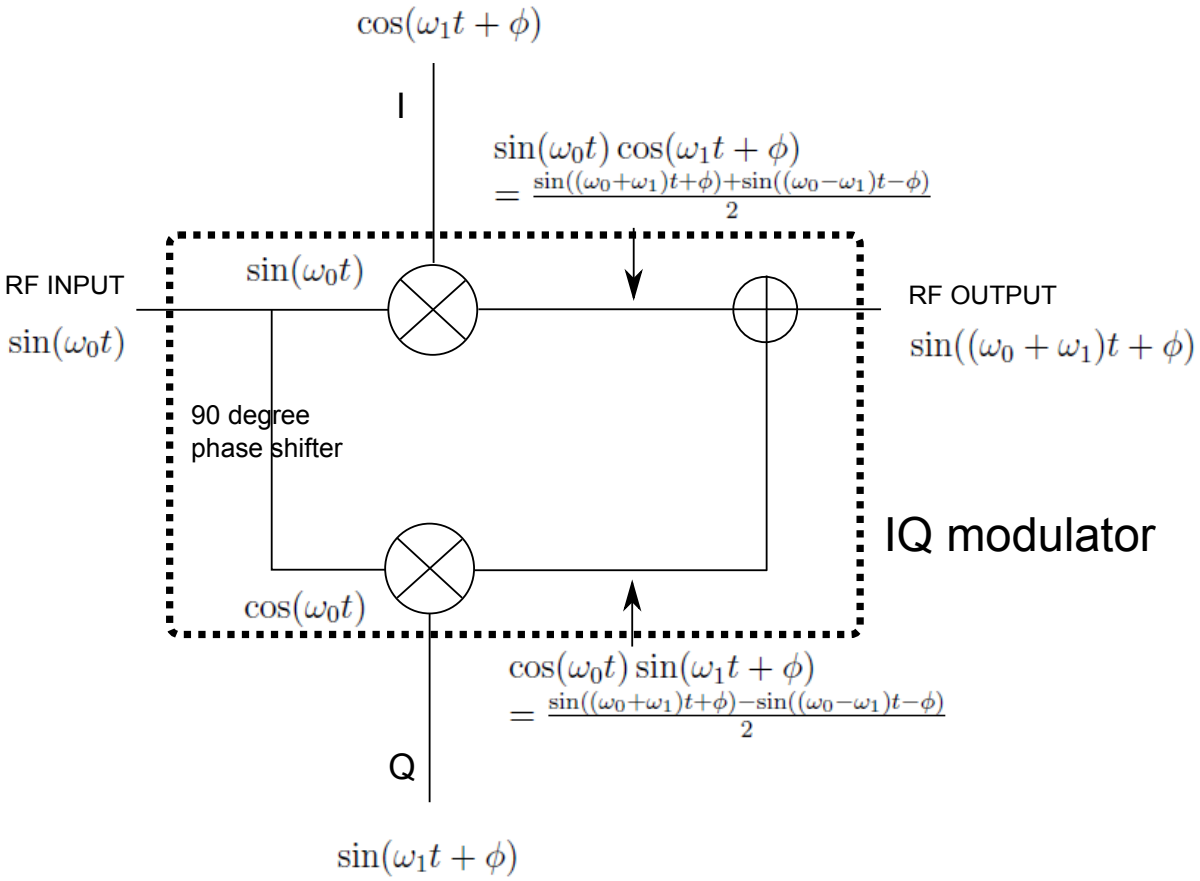

Figure 2.2: This illustrates how the IQ modulator is used in the spectrometer to avoid the power nonlinearity issue that would cause error in the phase of the output of the modulator. The inputs to both I and Q channels have the same power but with a 90° difference in phase. The output of IQ is the sum of the two channels. In this case, the output is $\sin((\omega_0 + \omega_1)t + \phi)$. Note that $\omega_0 + \omega_1$ is the ESR frequency and the ϕ is the desired phase of the output.

2.2 Resonator

The resonator used for the experiments is a 2-loop-1-gap aluminum resonator based on the idea from Eaton et al[17]. Figure 2.3 shows the dimensions of the resonator. The sample of interest sits in the small loop.

The resonator is placed inside a aluminum box and the microwave is coupled in by a small section of wire (inner conductor of coax) acting as an antenna. A tuning screw is placed on the opposite site of the antenna for adjusting the resonance frequency (illus-

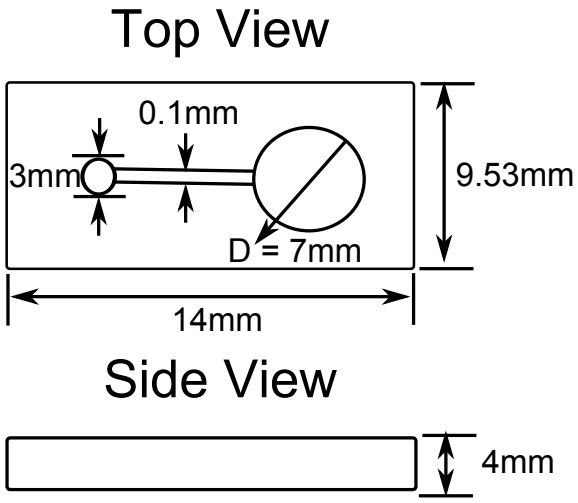

Figure 2.3: Resonator dimensions

trated in Figure2.4). The directions of the electric and magnetic fields in the resonator are illustrated in Figure 2.5.

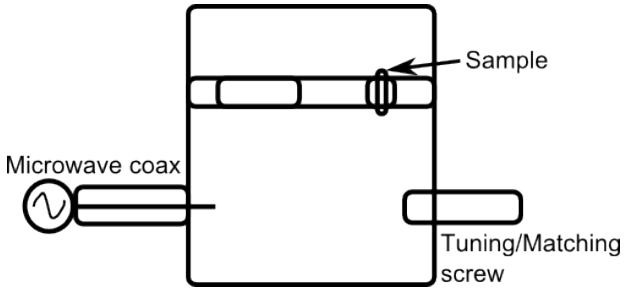

Figure 2.4: Resonator coupling scheme

For the current experiment setup, the largest distance between two accessible transitions is roughly 130MHz. This means in order to control the system, a minimum of 130MHz is required for the bandwidth of the resonator. The original resonator has a Q of around 300 and resonates at about 9GHz. This yields a bandwidth of roughly 30MHz. In order to meet the requirement on the bandwidth, a suitable amount of dielectric is added into the gap of the resonator to spoil the Q. In this case, Stycast 2850 (a type of epoxy) is used due to its stability after cure. The final bandwidth of the resonator measured in vector network analyzer (VNA) is 170MHz. Note that any bandwidth between 30MHz and 170MHz can be achieved in principle with different amount of epoxy. Figure 2.6 and figure 2.7 show the

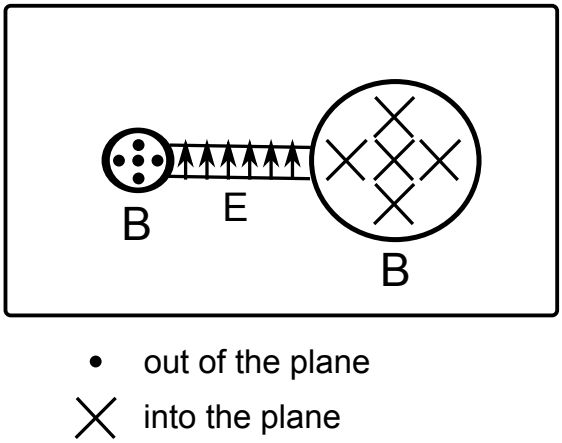

Figure 2.5: Electric and magnetic fields directions in the aluminum resonator

microwave reflection measurements before and after using epoxy, respectively.

2.3 Low temperature probe

The low temperature probe is designed based on three criteria:

1. The bandwidth of the resonator should remain roughly the same for all operational temperatures.
2. The sample can be cooled close to the temperature of the liquid cryogen (e.g. liquid helium or nitrogen).
3. The sample can be rotated about one axis at low temperature for sample orientation.

To fulfill the requirements, the probe is designed in such a way that the sample does not directly contact the cryogen, but instead is cooled by conduction through a cold finger. This prevents the resonator from touching the cryogen to maintain the temperature (and thus the bandwidth) of the resonator while cooling down the sample.

The cold finger contains a copper base that directly contacts the cryogen and a copper rotary piece that sits inside the copper base. Below the base is a copper cap that keeps the rotary piece in place. The sample is glued on one end of a quartz rod which is silver pasted onto the rotary piece. The sample also sits in the small loop of the resonator. The reason for having a quartz rod is to make sure the copper does not get too close to the resonator to

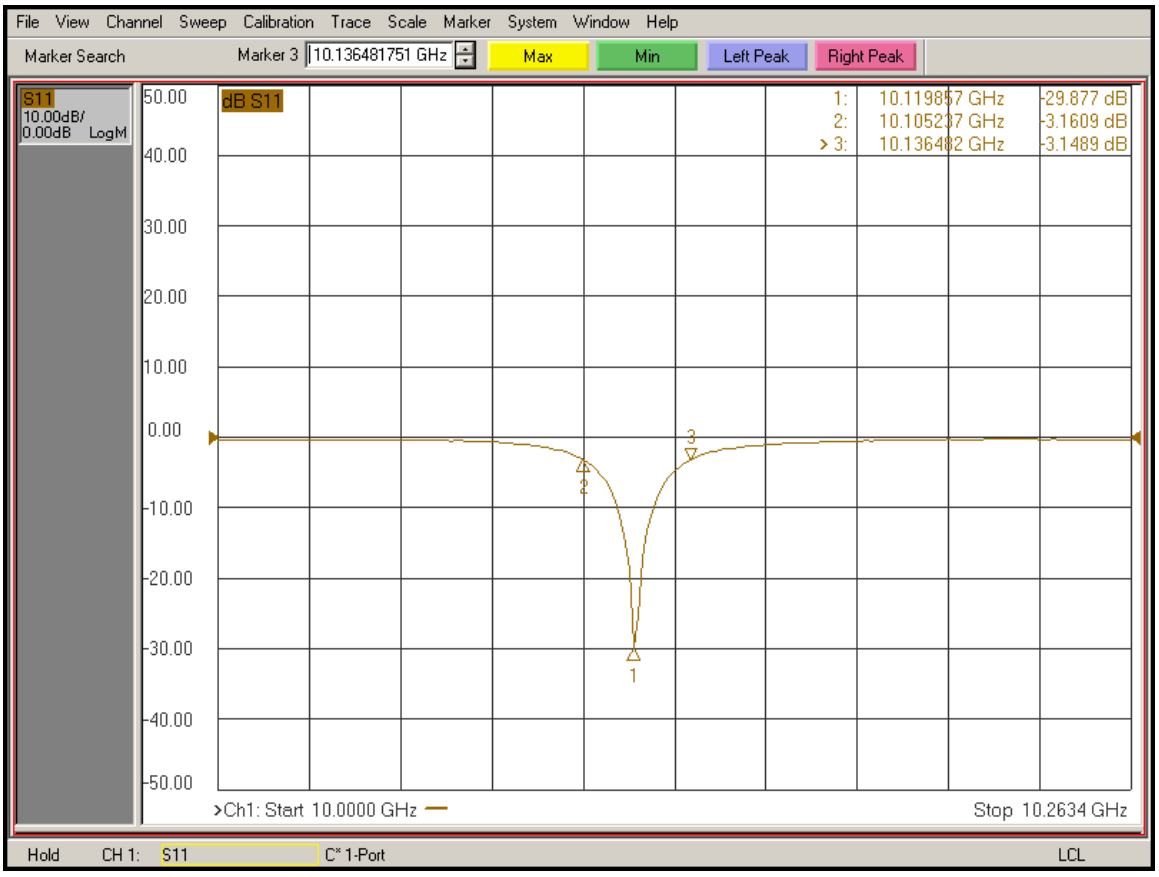

Figure 2.6: Reflection measurement of the resonator using vector network analyzer (VNA) before applying epoxy, the bandwidth of the resonator is 31MHz.

interfere with the microwave magnetic field, e.g. to make the field inhomogeneous around the sample. Quartz and silver paste are chosen due to their high thermal conductivity. To have the best thermal conductivity between the copper base and the rotary piece, the rotary piece is machined to fit in the copper base with maximal contact surface area. In order to be able to rotate the rotary piece, hence the sample, the copper base and the rotary piece are both machined carefully to have the best quality surfaces to reduce the friction. Figure 2.8 shows a diagram of the cold finger assembly.

The rest of the probe contains a resonator box that hosts the resonator, a microwave input/output port and a pick-up antenna for "pulse fixing" (see chapter4 section4.1), a worm gear set that is used to rotate the sample, a tuning/matching mechanism, two temperature sensors (mounted on the cold figure and the resonator box) and a vacuum box that encapsulates the whole assembly. Figure 2.9 shows a CAD drawing of the whole setup.

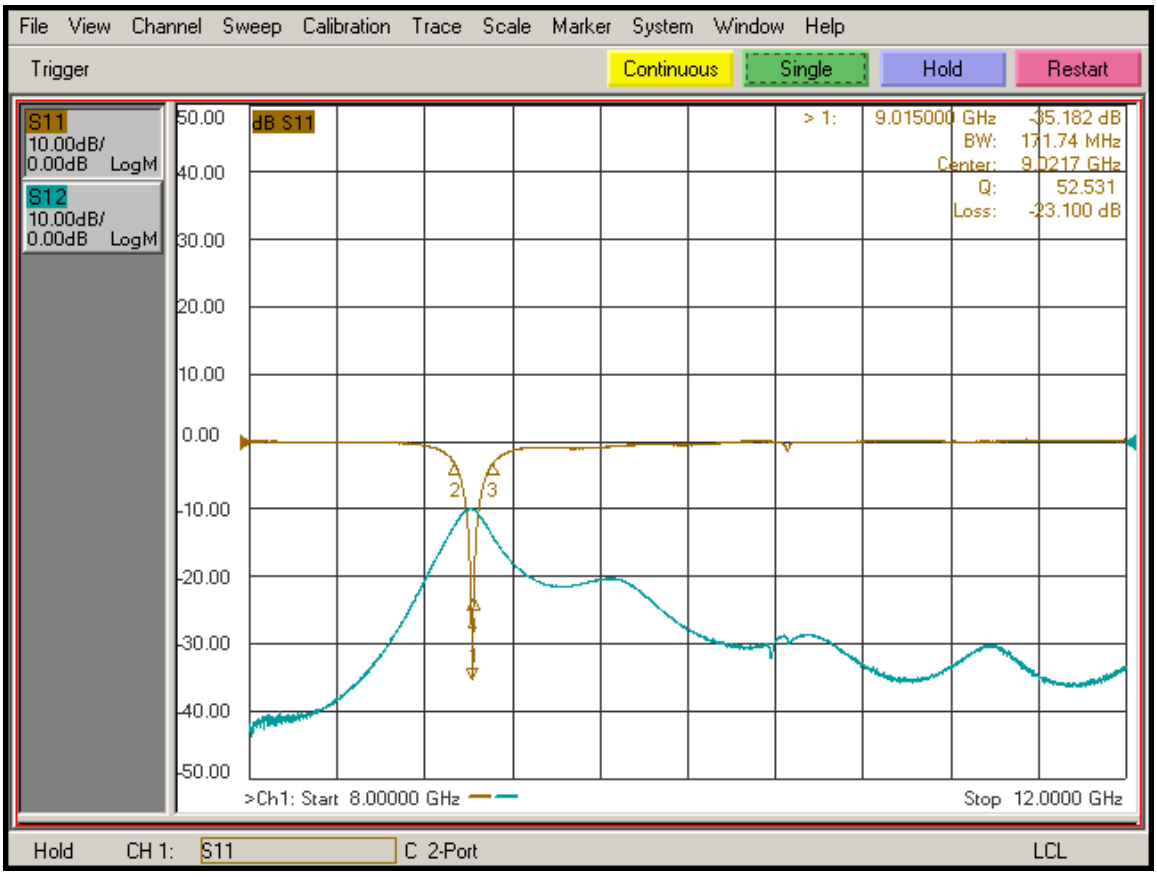

Figure 2.7: Reflection measurement of the resonator after applying epoxy using VNA, the bandwidth of the resonator is now 170MHz. Notice that the resonance frequency is also shifted downward by roughly 1GHz. The blue line shows the transmission efficiency of a pickup coil that is used to examine the input pulses to the resonator.

This probe has been tested under liquid nitrogen and liquid helium conditions. The test results for liquid nitrogen for resonator bandwidth, sample temperature and the ability for sample rotation are as follows.

2.3.1 Resonator bandwidth

The bandwidth of the resonator is crucial for doing quantum computing in ESR, therefore is a high priority while designing the probe. The main factor that changes the resonator bandwidth in the current setup is the temperature of the resonator, e.g. at cryogenic temperatures, bandwidth expected to decrease dramatically as Q increases (due to the

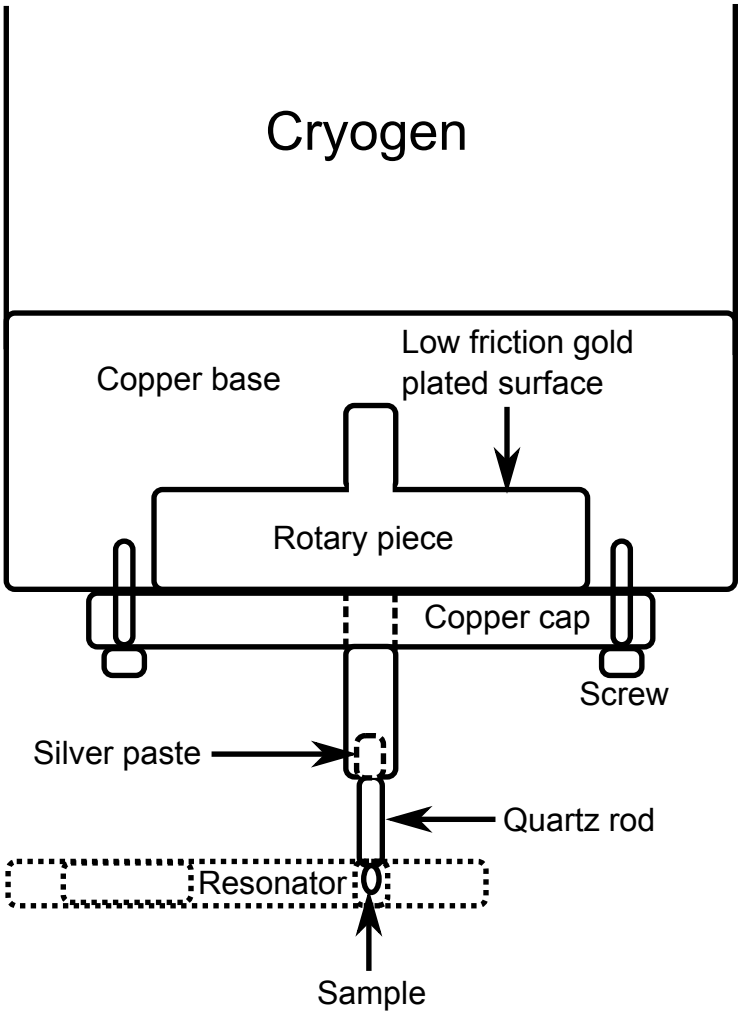

Figure 2.8: This shows the cold finger assembly. The copper base is in contact with the liquid cryogen from the top. The sample sits inside the resonator.

decrease in the resistance of Aluminum). Due to the irradiative heating between the sample and the resonator, the temperature of the resonator decreases somewhat as the sample cools. The final stable temperature of the resonator is around 260K. Although the final temperature of the resonator is 40K below room temperature, the change in bandwidth is roughly 0. Note that re-tuning is required after the temperature of the resonator stabilizes. The resonance still stays at the same frequency after re-tuning.

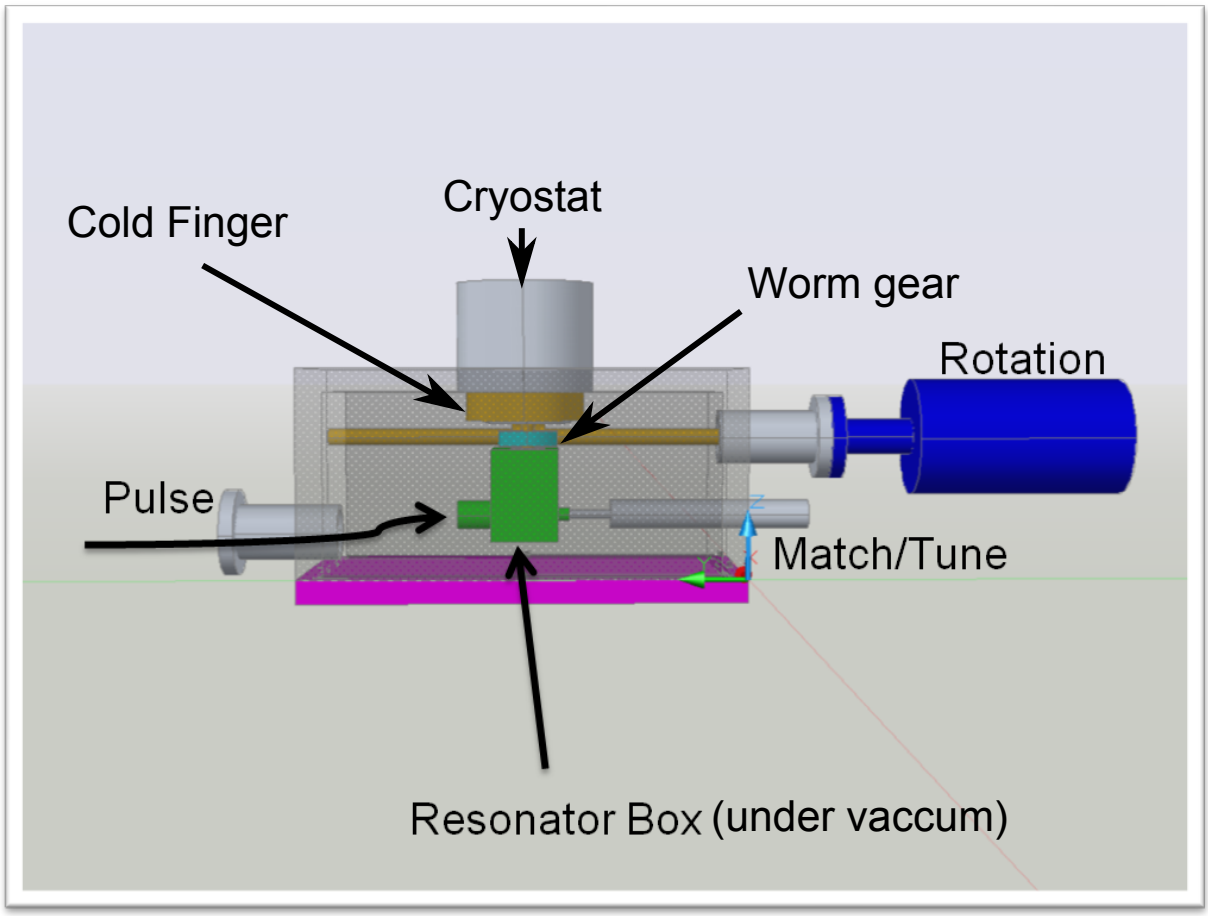

Figure 2.9: The CAD drawing of the entire low temperature probe.

2.3.2 Sample temperature

Due to irradiative heating, the sample temperature is typically about 10K above the temperature of the cryogen used. This is calculated by measuring the ESR signal level and the coherence time T_2 of the sample as we now describe. The intensity of the signal from a spin system with transverse magnetization is proportional to the population difference between the spin-up and spin-down states of the electron in its thermal state. The population difference is proportional to the inverse of the temperature and is described by equation A.4. It can be approximated as

$$n_{\uparrow} - n_{\downarrow} = \frac{A}{T} \tag{2.1}$$

where $n_\uparrow$ is the population of the spin-ups, $n_\downarrow$ is the population of the spin-downs, A is a constant and T is temperature in Kelvin.

The other factor that changes the signal intensity is the spin coherence time T2. The signal intensity decays with respect to the time t between the moment the coherence is created in XY plane to the point when the signal is measured. The decay rate is $e^{-t/T2}$ and T2 is temperature dependent.

The equation that describes the relationship between the temperature and the signal intensity $G(t)$ is:

$$G(t) = \frac{A}{T} e^{-t/T2} \tag{2.2}$$

At room temperature, signal intensity is measured to be 2.9 times smaller than the signal intensity with liquid nitrogen. T2 is measured to be 4.6μs and 2.1μs for room temperature test and liquid nitrogen test, respectively. These yield an effective sample temperature of 87K (10K above the cryogen temperature).

2.3.3 Ability to orient the sample

It is important to have the ability to rotate the sample in situ since the spin Hamiltonian depends strongly on the sample orientation. It is also recognized that mapping out the spectra as a function of orientation helps determine the spin Hamiltonian.

To have the sample rotate properly, the contacting surfaces of the copper base and the rotary piece should both be clean and smooth. The screws holding the cap onto the copper base should not be over tightened. Whether the sample can be rotated can be immediately determined by attempting to rotate the sample with the rotation assembly. For the rotation to work at low temperature, the sample should rotate smoothly without any noticeable friction at room temperature.

For the current malonic acid sample, there are four allowed transitions that can be seen through a fieldswept experiment where the ESR frequency is fixed while the static field is varied. The allowed transitions would show up in the resonance spectrum as peaks indicating the transitions can be driven with the corresponding fields at the particular frequency. The locations of the peaks are determined by the hyperfine couplings, and the coupling coefficients are functions of the sample orientation. By measuring the fieldswept data with respect to the orientation, the ability for sample rotation can be tested accurately. Figure 2.10 shows a typical plot of the fieldswept data and figure 2.12 shows theoretical and experimental values of the spacings (couplings) versus the angle of the sample being rotated about the y-axis of the sample. The experimental data agrees with the theoretical one. This means the sample can be rotated precisely within experimental errors.

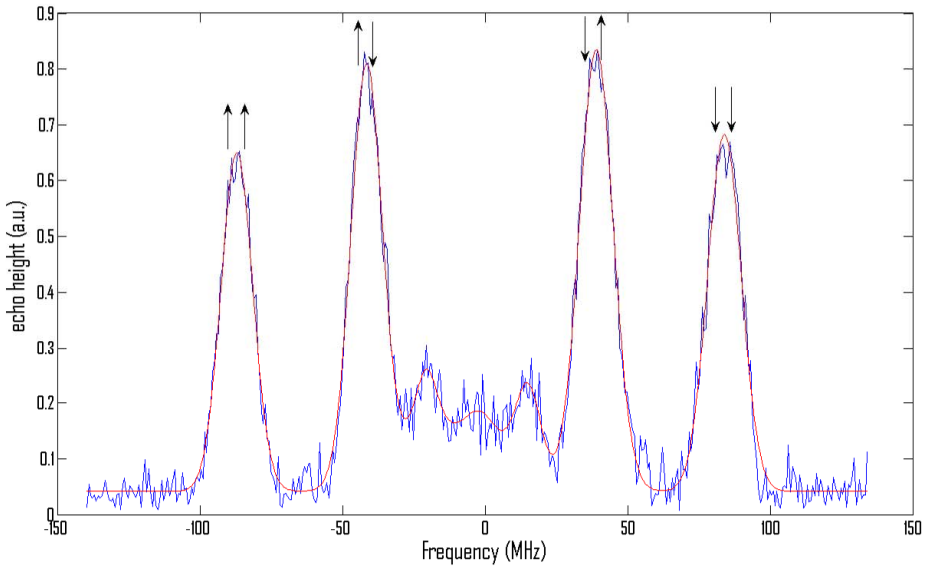

Figure 2.10: A typical fieldswept data showing the four allowed transitions. The arrows above the peaks indicate the spin states of the two nuclear spins at the corresponding transitions. The blue line is the raw data that measures the echo height. The pulse sequence is shown in Figure2.11. Four peaks can be fitted to the raw data and is showing as the red curve.

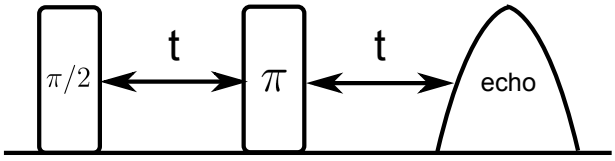

Figure 2.11: Pulse sequence of the fieldswept experiments (also standard spin echo measurements). τ is a constant.

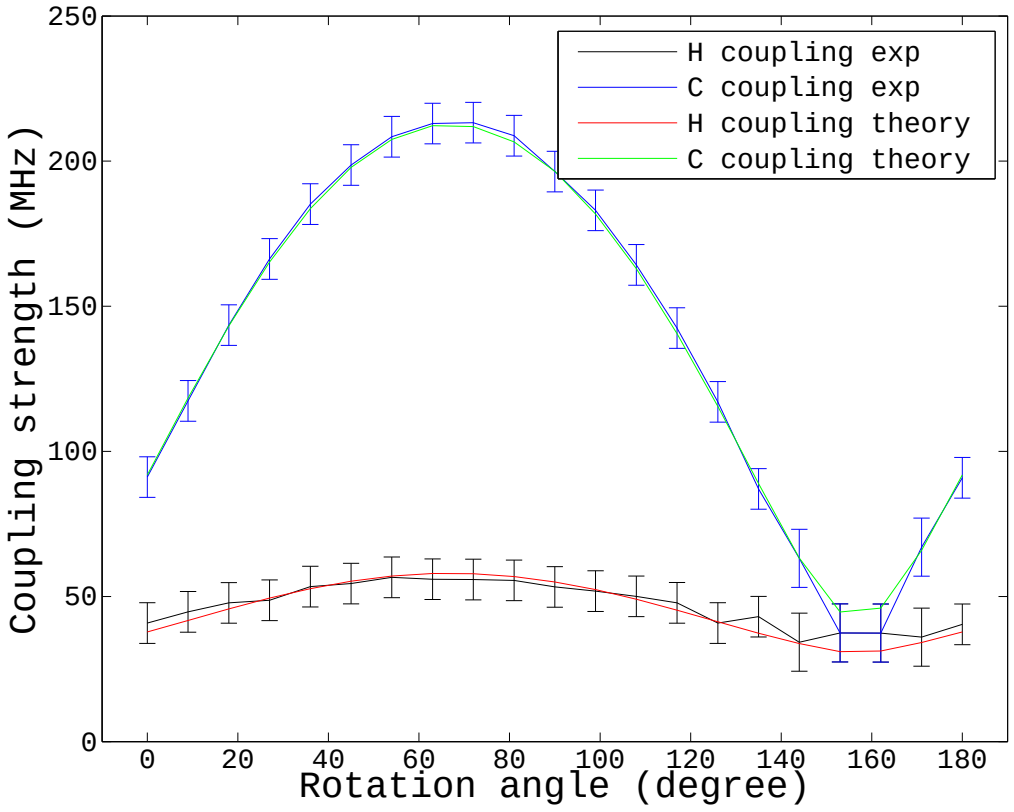

Figure 2.12: Peak splittings from fieldswept data (H coupling is the splitting between $|\uparrow\uparrow\rangle$ and $|\uparrow\downarrow\rangle$ and C coupling is the splitting between $|\uparrow\uparrow\rangle$ and $|\downarrow\uparrow\rangle$ in fig2.10). The angle indicates the amount of rotation done to the sample about y-axis of the crystal. The theoretical values are calculated based on the hyperfine tensor measure by Cole and Heller[4].

Chapter 3

Spin System

3.1 Single crystal malonic acid

The sample used in experiments is a single crystal of malonic acid. Figure 3.1 shows a drawing of the molecule. One reason for choosing this as the sample is that malonic acid is well-studied[2][14][1]. The space group for malonic acid is $P\bar{1}$[9] (two molecules per unit cell and they are related by mirror symmetry) so that every spin in every molecule in the sample feels the same environment. Section 3.1.1 describes the sample preparation procedures.

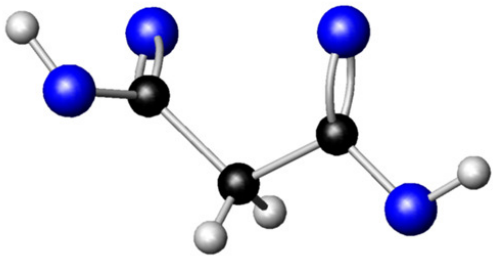

Figure 3.1: Malonic acid molecule[15]. White balls represent proton atoms, black balls represent carbon atoms and blue balls represent oxygen atoms.

3.1.1 Sample preparation

In order to have one electron and two nuclear spins in the system, malonic acid with the methyl carbon labeled is used. The chemical formula of such molecule is $COOH-{}^{13}CH_2-COOH$. The substance is then dissolved in water. By controlling the evaporation speed of water, single crystals can be grown from the solution. Adding in seed crystal when the solution is saturated helps in getting better quality and larger crystals.

In order to get an unpaired electron in the system, X-rays are used to irradiate the crystal[14]. To get a decent amount of electron defects in a 1mm $\times$ 1mm $\times$ 3mm crystal, an X-ray single crystal diffractometer from Bruker AXS is used to shine X-ray on the crystal for $\sim$20 hours. During this process, proton-carbon bonds get destroyed and leave unpaired electrons. Most of the radicals created are not stable. After annealing the sample at 60^oC for 24 hours, only one type would be present in measurable amounts. The chemical formula of the stable radical is $COOH-{}^{13}\dot{C}H-COOH$. Note that electron, proton and ${}^{13}C$ all have spin-1/2.

3.1.2 Different isotopologues

Different isotopologues of malonic acid are also considered as sample candidates. A major draw-back from the sample $COOH-{}^{13}\dot{C}H-COOH$ is the broad linewidth of the ESR peaks (14MHz) due to the dipole-dipole coupling between the electron and the protons in the environment[6] (i.e. the carboxylic protons and the protons on the methyl groups without free electrons). The dipole-dipole coupling strength depends on the gyromagnetic ratios of the two coupled spins as follows[13]:

$$d_{jk} = -\frac{\mu_0}{4\pi}\frac{\gamma_j\gamma_k\bar{h}}{r_{jk}^3}\frac{1}{2}(3\cos^2\Theta_{jk}-1) \tag{3.1}$$

where μ_0 is the magnetic constant, γ_j and γ_k are the gyromagnetic ratios of the two spins, r_{jk} is the distance between the two spins and Θ_{jk} is the angle between the vector connecting the two spins and the external magnetic field.

The easiest way to reduce the coupling strength is to replace the atoms with the ones that have smaller gyromagnetic ratios. In this case, in order to maintain the molecular and crystal structure, it is the best to use deuterium atoms to replace the protons. The chemical formula of this 1e-2n 3-qubit system is $COOD-{}^{13}\dot{C}H-COOD$. Now, since half of the protons close to the free electron are replaced by deuterium, the linewidth would be reduced by 50% (or 7MHz). While the partially deuterated sample seems to be an ideal sample to use, there is not a known way to make the sample. Several attempts have been made by us trying to exchange the carboxylic protons with deuteriums in solution, unfortunately

spins	chemical formula	calculated linewidth	studied in this work
$e-H-^{13}C$	$^{13}\dot{C}H(COOH)_2$	14MHz	yes
$e-H-^{13}C$	$^{13}\dot{C}H(COOD)_2$	7MHz	no
$e-D-^{13}C$	$^{13}\dot{C}D(COOD)_2$	2MHz	yes

Table 3.1: Comparison between the sample that is currently being examined, the ideal sample and the two-qubit-one-qutrit sample. The calculation is done by summing over interactions between the electron and its 500 closest nuclear spins (including more nuclear spins doesn't make much difference in the result). The linewidth is not orientation dependent.

the methyl proton also exchanges with the surroundings relatively easily. This leads to end-products containing mixtures of $COOH-^{13}\dot{C}H-COOH$, $COOD-^{13}\dot{C}D-COOD$ and $COOD-^{13}\dot{C}D-COOD$.

Although $COOD-^{13}\dot{C}H-COOD$ is not accessible, fully deuterated malonic acid $COOD-^{13}\dot{C}D-COOD$ can be prepared. Since all the spins around the free electron are deuterium for the fully deuterated sample, the linewidth is 6.5 times smaller than the fully protonated sample (the gyromagnetic ratio of deuterium is 6.5 times smaller than that of proton). Instead of having three qubits, this sample consists two qubits and one qutrit since deuterium is spin-1 particle. A potential problem of this sample is the additional quadrupole coupling term in the spin Hamiltonian[18][10]. It is still believed that with careful design, interesting experiments can be performed on this sample. We reserve this for future work.

Table 3.1 shows a comparison between the three samples.

3.2 Malonic acid characteristics

To lay a groundwork for the experiments, some key characteristics have been measured for this sample.

3.2.1 Relaxation times

The relaxation times T_1 and T_2 are very important for designing experiments. T_1 is measured using the inversion recovery method and T_2 is measured using a two-pulse ESEEM (electron spin echo envelope modulation) experiment. Typical values of T_1 and T_2 at liquid Nitrogen temperature are $\sim 20\mu$s and $\sim 2\mu$s, respectively. Note that both T_1 and T_2 depend on the orientation of the crystal with respect to the static magnetic field. Figure

3.2 shows a plot of typical T_1 data, figure3.3 shows the pulse sequence for measuring T1 and figure 3.4 shows a plot of typical T_2 data.

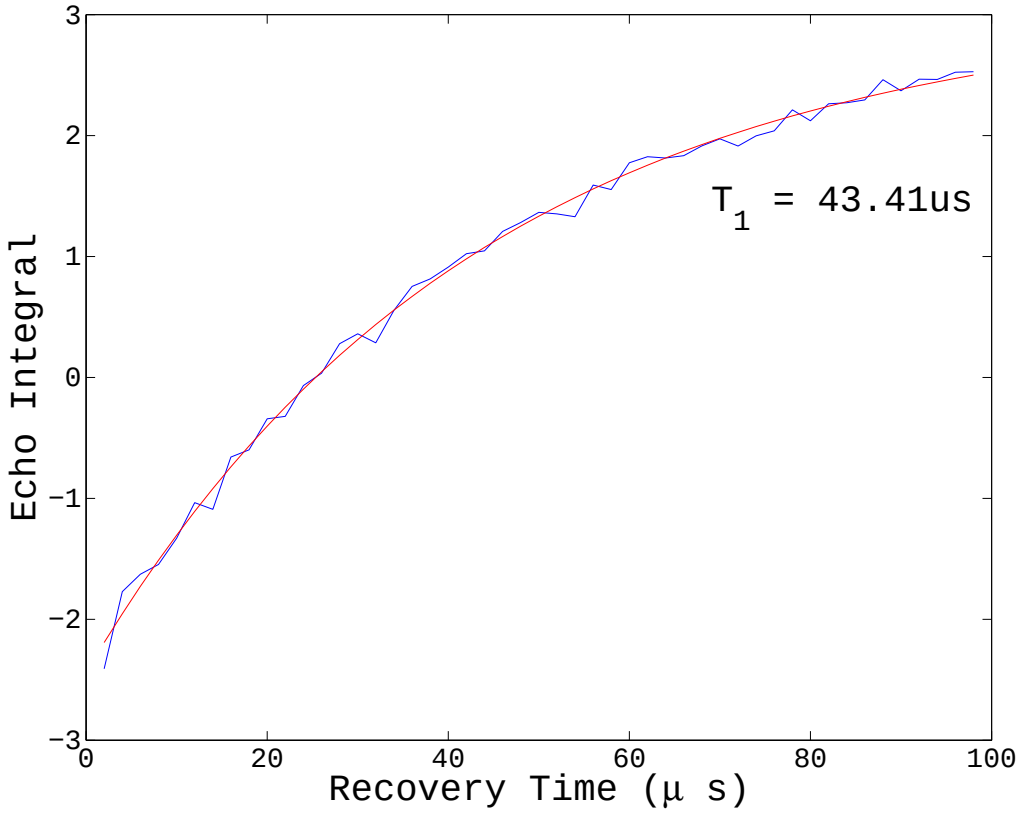

Figure 3.2: T1 measured via inversion recovery at liquid nitrogen temperature

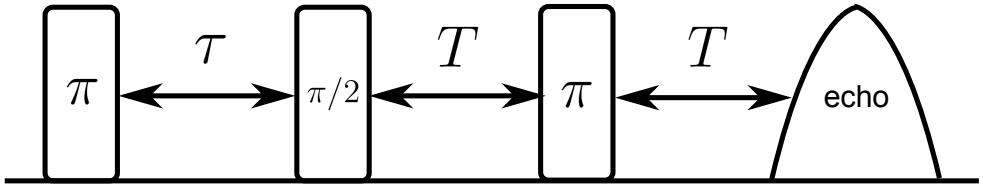

Figure 3.3: Pulse sequence of the T1 experiments. The first π pulse inverts the spin population. τ is a variable. T_1 can be measured by fitting an exponential function to the data.

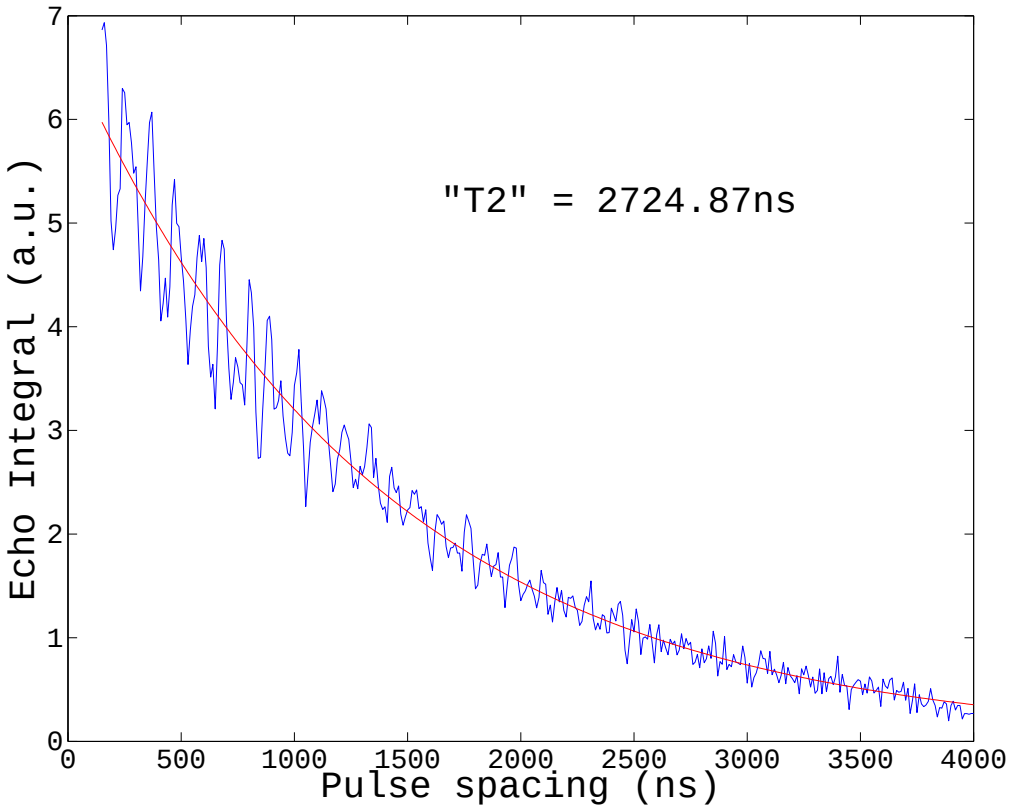

Figure 3.4: T2 measured via two-pulse ESEEM at liquid nitrogen temperature. The pulse sequence for this measurement is the same for fieldswept (see figure2.11), where τ in this case is a variable. Note the modulations come from the nuclear frequencies of the spin system.

3.2.2 Spin Hamiltonian

The spin Hamiltonian of the system has the form

$$\mathcal{H}_0 = \omega_S S_Z + \omega_C I_{CZ} + A_C S_Z I_{CZ} + B_C S_Z I_{CX} + \omega_H I_{HZ} + A_H S_Z I_{HZ} + B_H S_Z I_{HX} \quad (3.2)$$

The hyperfine tensor of the system was found by Cole and Heller in 1961[4]. The forms of electron-proton and electron-carbon hyperfine tensors in coordinates system of figure 3.5 are as follows:

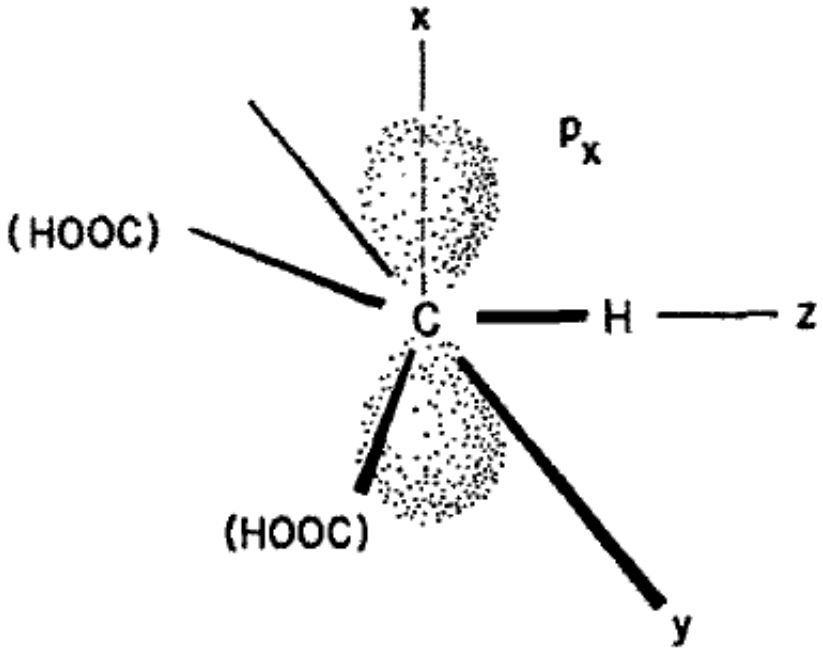

Figure 3.5: Malonic acid Cartesian molecular coordinates system[4]

$$e-H: \begin{pmatrix} -58 & 0 & 0 \\ 0 & -91 & 0 \\ 0 & 0 & -29 \end{pmatrix} MHz \tag{3.3}$$

$$e-^{13}C: \begin{pmatrix} 212.7 & 0 & 0 \\ 0 & 22.8 & 0 \\ 0 & 0 & 42.2 \end{pmatrix} MHz \tag{3.4}$$

By varying the orientation of the crystal, the hyperfine couplings can be adjusted (rotate the hyperfine tensor with rotation matrices, see details in Appendix B). It is wise to choose an orientation that enables strong transitions between all eigenstates but also has not too large bandwidth. An orientation that is easily distinguishable and also has good transition probabilities between all states is chosen for the experiments. The hyperfine couplings for this orientation (the three angles needed to rotate the sample to this orientation B are 98°, 12.5° and -70°) are

$$A_C = 61.2MHz,\ B_C = 55.6MHZ,\ A_H = -35.9MHZ \text{ and } B_H = 16.3MHz \tag{3.5}$$

In order to verify that the spin Hamiltonian is equal to the desired one, several tests are required. In principle, one three pulse ESEEM spectrum (see figure 3.6 for the pulse

sequence) is enough to determine the spin Hamiltonian[19]. The positions of the peaks in three pulse ESEEM spectrum are functions of the isotropic and anisotropic coupling terms As and Bs. When all peaks can be clearly seen in the spectrum, the As and the Bs can be calculated. Usually, however, the peaks representing couplings between the electron and the carbon-13 have much smaller intensities, only the A and B for electron and proton can be determined from one three pulse ESEEM measurement. In order to determine the spin Hamiltonian precisely, three measurements with different sample orientations (but all on the same sample rotation axis) should be performed. From the three pieces of data, the rotation axis can be first found by mapping the measured data to simulated data. Once the rotation axis is found, the A and B coupling constants for electron and carbon-13 can be extracted from the simulated data. Figure3.7 shows the three pulse ESEEM data the chosen orientation (98,12.5,-70) and figure3.8 shows the Fourier transform of the ESEEM data.

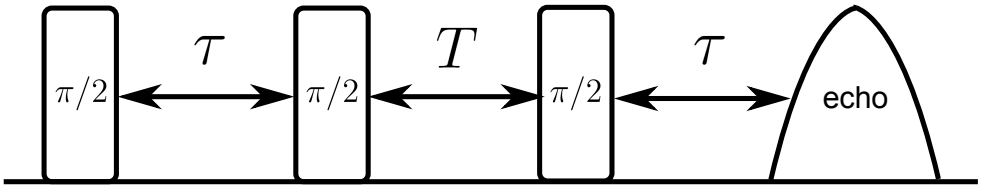

Figure 3.6: Pulse sequence of three pulse ESEEM experiments. τ is a constant. T is the variable.

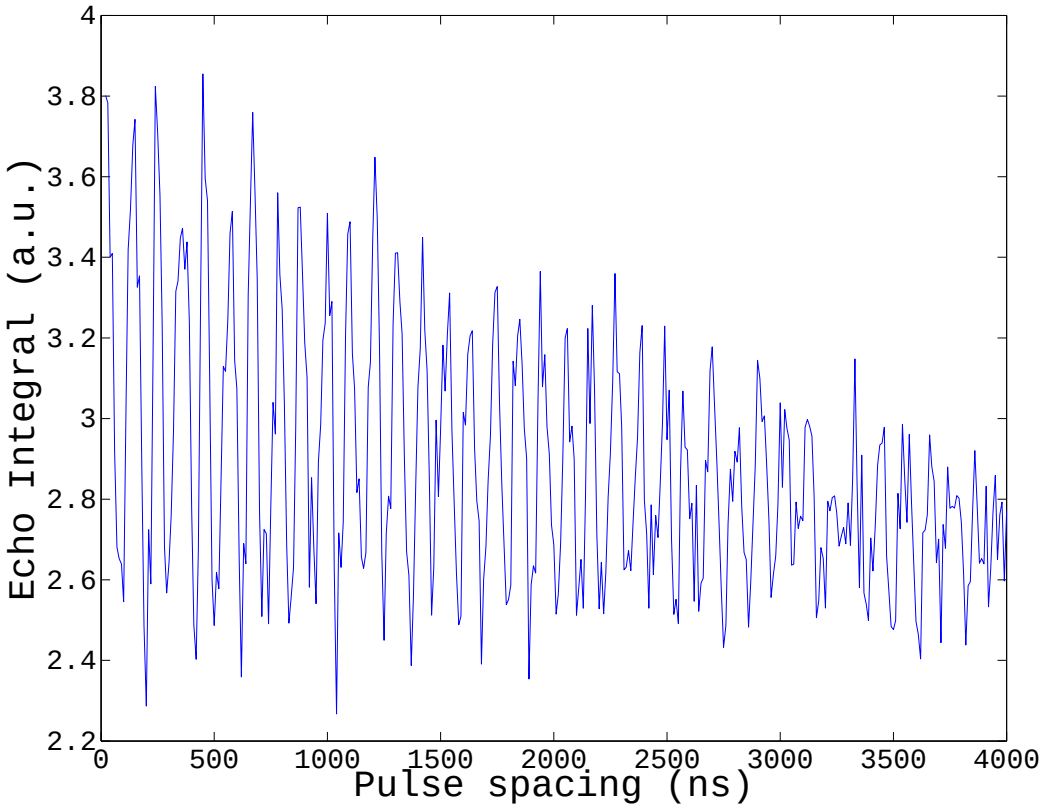

Figure 3.7: The three pulse ESEEM data at the chosen orientation. In order to get to the orientation, the sample needs to be rotated 98° about the sample's y axis, then 12.5° about the sample's z axis and then -70° about the sample's y axis.

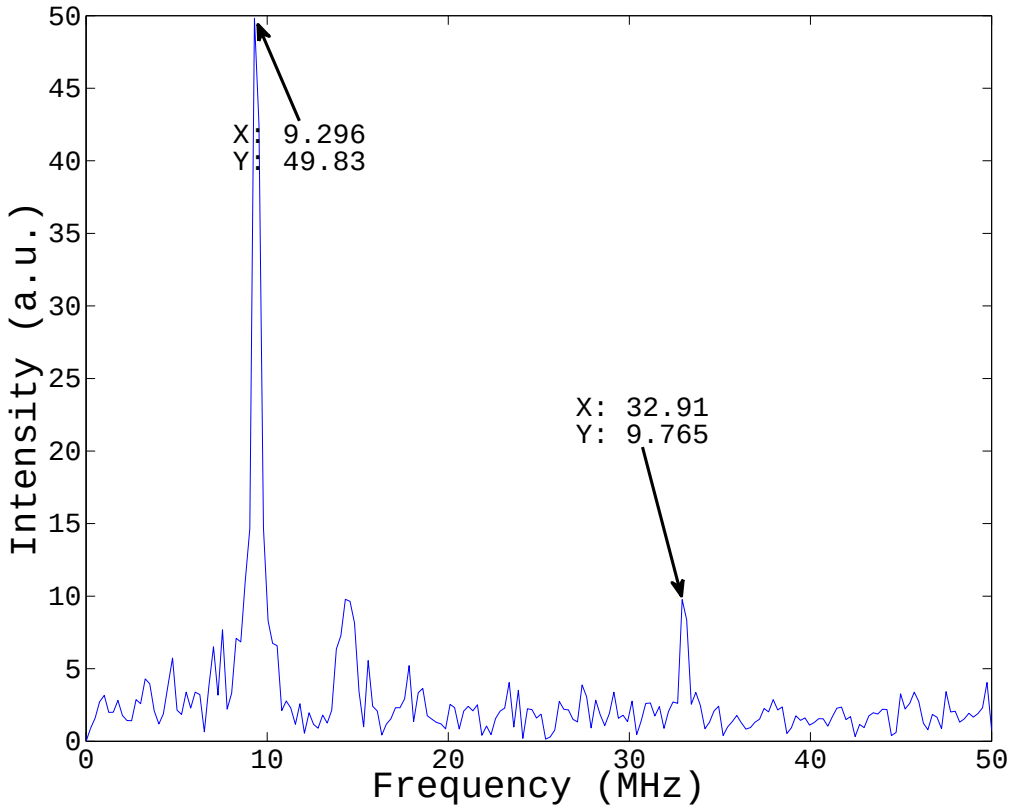

Figure 3.8: Fourier transform of the three pulse ESEEM data from figure3.7. The two labeled peaks can be used to determine the electron-proton hyperfine couplings.

Chapter 4

Experiments

The goal of the experiments is to demonstrate universal control in the 3-spin malonic acid system. Section4.1 illustrates necessary steps before performing experiments, section4.2 shows the simulations of the experiment.

4.1 Preparation for experiments

In order to have high fidelity control, GRAPE pulses need to be designed based on the following criteria:

1. the pulse length needs to be as short as possible so that decoherence can be minimized.
2. the pulse should be robust against a certain range of Hamiltonian distribution (i.e. uncertainty in the electron Zeeman energy) since the inhomogeneous linewidth of a transition is 14MHz.
3. the bandwidth of the pulse should be within the bandwidth of the resonator so that the pulse can be corrected for non-linearities in pulse generation ("pulse fixing") and implemented with high fidelity.

The pulse finding is done by the ESR pulse finder program written by Dr. Colm Ryan. Pulse fixing is done through feedback control by comparing the actual pulse seen by the sample (detected through a pickup coil) with the ideal pulse. Figure 4.1 shows the in-phase component of a pulse that performs a NOT gate on electron spins and the in-phase component of the same pulse after pulse fixing. The final fixed pulse closely resembles the ideal pulse (this can also be seen from figure 4.2, which shows the spectra of both ideal and fixed pulses). This makes sure minimal fidelity loss is due to the imperfect implementation of the GRAPE pulses.

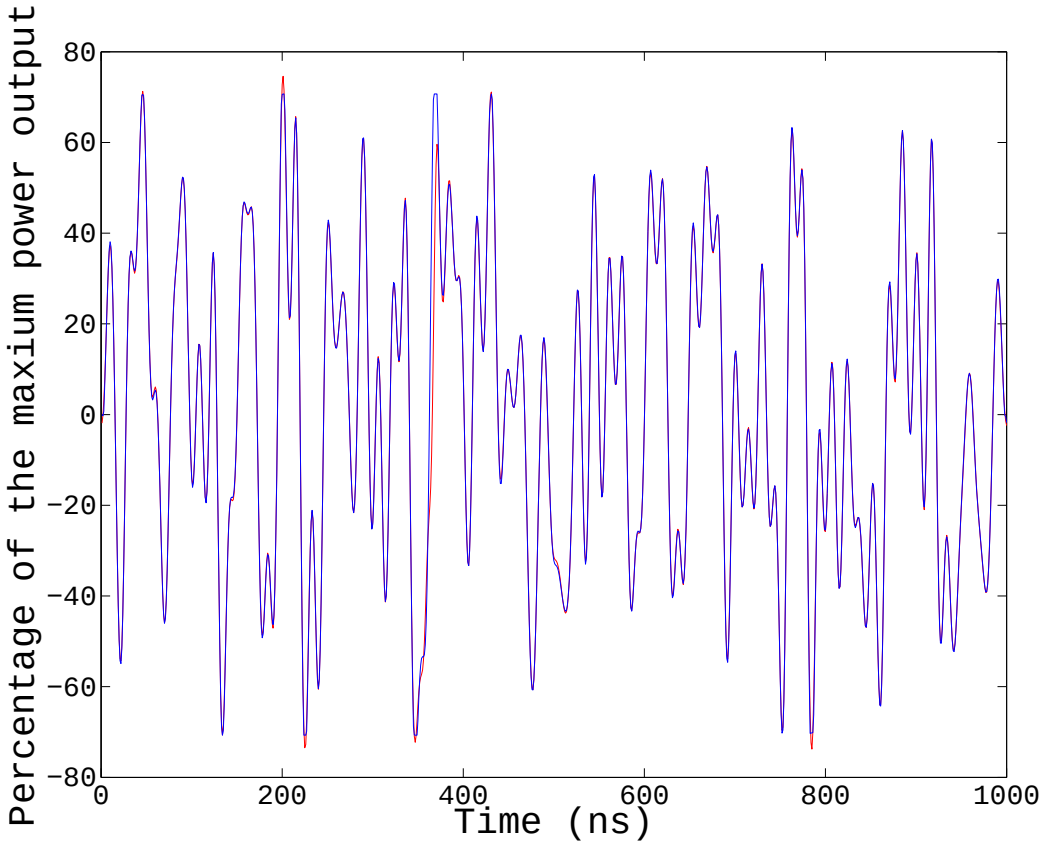

Figure 4.1: In-phase components of the ideal pulse (blue) and the measured pulse after pulse fixing (red). Pulse fixing enables the pulse to be used closely resembles the ideal pulse. The small differences between the two are results of the limited bandwidth of the resonator.

4.2 Simulations

To show universal control, three different GRAPE pulses are designed. One is a π pulse which does a NOT gate for the electron. The other two are to perform controlled-NOT gates with one having the proton being the control bit and the carbon being the target bit and the other using carbon to control proton. All three pulses are robust against 10MHz uncertainty in electron Zeeman energy. The first experiment would utilize the π pulse and demonstrate control over the electron transitions and the second would use the two

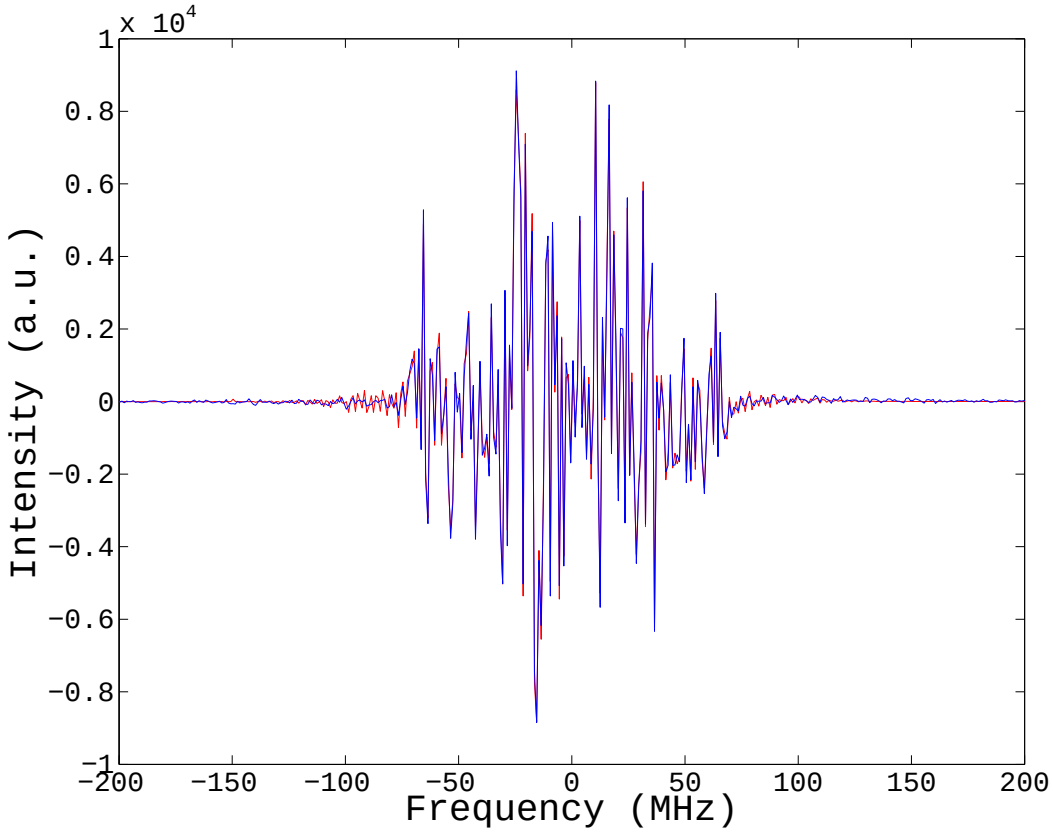

Figure 4.2: Spectra of the ideal pulse (blue) and the measured pulse after pulse fixing (red).

control-NOT pulses to demonstrate control over the nuclear transitions. Figures 4.3, 4.4 and 4.5 show the transitions the three pulses would drive respectively.

For the first experiment, the initial state of the system is in the thermal state. The spin populations are higher in the four states with lower energies. By applying a $\pi/2$ hard pulse on all transitions, the population differences can be measured. When the GRAPE pulse is applied to the system before the readout pulse, the populations of the electron spin-down and spin-up states are swapped. Applying the readout pulse would then yield the same population differences but with an opposite sign. Figures 4.6 and 4.7 show the spectra of the system measured in thermal state, and measured after the GRAPE pulse, respectively, with no uncertainty in electron Zeeman energy. The peak intensities and the

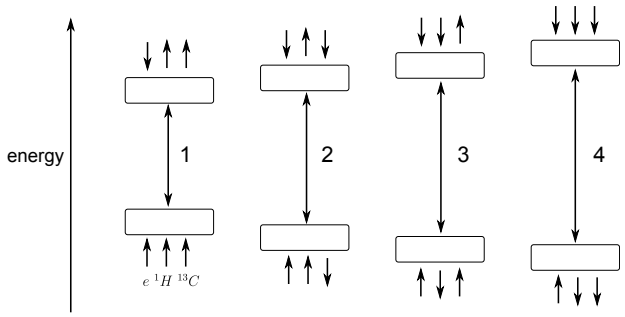

Figure 4.3: Transitions driven by the GRAPE π pulse. The arrows from the left to the right indicate the spin state of the electron, proton and carbon respectively.

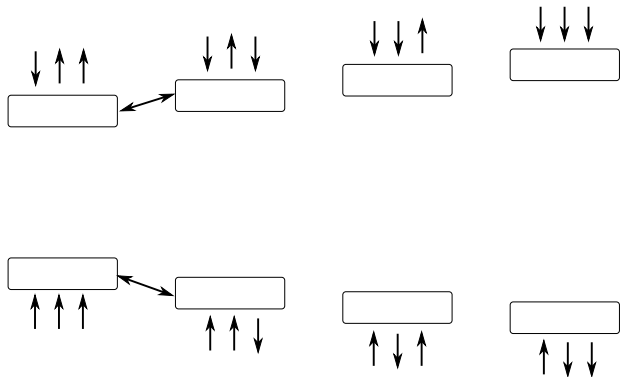

Figure 4.4: Transitions driven by the GRAPE proton control-NOT pulse. The arrows from the left to the right indicate the spin state of the electron, proton and carbon respectively.

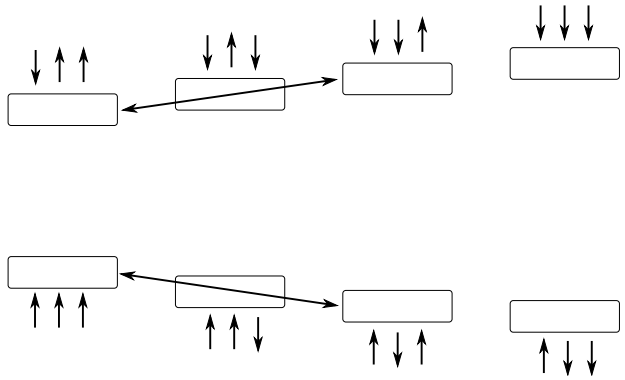

Figure 4.5: Transitions driven by the GRAPE carbon control-NOT pulse. The arrows from the left to the right indicate the spin state of the electron, proton and carbon respectively.

peak number		reference	with GRAPE π pulse	difference
1	phase	-126.2	53.4	179.6
	intensity	10418	7449	-28.5%
2	phase	-97.6	81.7	179.3
	intensity	10378	7386	-28.8%
3	phase	-82.4	98.1	180.5
	intensity	10378	7125	-31.3%
4	phase	-53.8	126.7	180.5
	intensity	10418	7316	-29.8%

Table 4.1: Comparison between simulated spectra (without Hamiltonian distribution and with $T_2 = 2.7\mu s$) taken with readout pulse only and with GRAPE π pulse, phase in degrees and intensity in a.u.

phases of the four peaks with and without the GRAPE pulse are listed in table 4.1. Note that the phase differences of the peaks with and without the GRAPE pulse are roughly 180°, which means the spin populations are successfully swapped. The peak intensities with the GRAPE pulse are ∼30% lower than the ones of the reference spectrum. This is due to the T_2 process during the GRAPE pulse time (the major source for signal loss) as well as the imperfect fidelity of the pulse. Note, the T_2 time used in the simulations is the experimentally measured value, 2.7μs, for the current setup. Figures 4.10 and 4.11 show the spectra of the system measured in thermal state, and measured after the GRAPE pulse, respectively, with 14MHz uncertainty in electron Zeeman energy (the measured linewidth of the peaks). Since the points defining the Zeeman distribution are discrete, line broadening is used. Table 4.2 lists the peak intensities and phases of the result with 14MHz Hamiltonian distribution.

If an infinite T_2 is assumed for the same experiment, the result would then be 99.4%. Figure4.8 and figure4.9 show the simulated results without Hamiltonian distribution. This means in principle, very high fidelity can be achieved by reduing the length of the GRAPE pulse and extending the coherence time (can be done by cooling the sample to lower temperature).

The second set of experiments are to test the control-NOT gates. The initial state of the experiment is a pseudo pure state with population difference on only the first transition (Figure 4.12). This is prepared by applying Gaussian selective $\pi/2$ pulses on transition 2,3 and 4, then waiting for a time of T_2. The $\pi/2$ pulses create coherences on the last three transitions. By waiting a time of T_2, decoherence makes the populations between electron spin-up and spin-down states even (strictly speaking, T_2 and T_1 processes compete during the delay. T_2 process kills the coherence between the two states while T_1 process tries to drive the population to the spin-up state. It is found that waiting a time of T_2 yields the

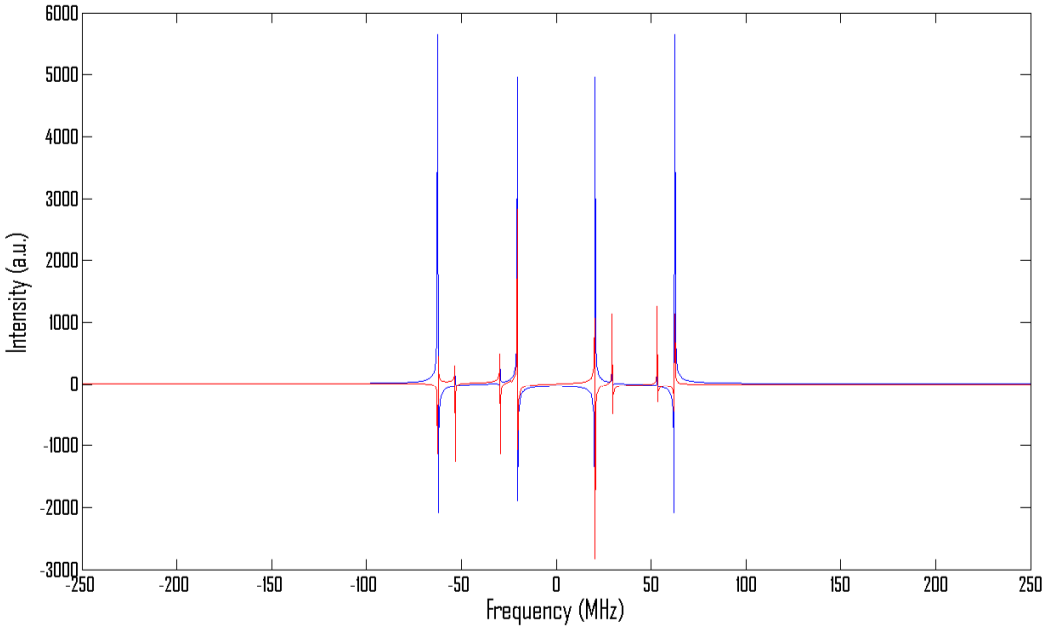

Figure 4.6: Simulated spectrum due to FID after a $\pi/2$ readout pulse without Hamiltonian distribution with $T_2 = 2.7\mu s$. Blue is the real component of the spectrum, red is the imaginary. Note that the four peaks are not all in phase. This is because the Fourier transform does not start exactly at the beginning of the FID since the smallest time step size is 1ns in simulations.

best result for preparing pseudo-pure state). If a control-NOT gate is applied before the detection, the population difference on the first transition would then be shifted to another transition depending on the control-NOT gate used. Figure 4.13 shows the spectrum of the pseudo pure state of the system, and figures 4.14 and 4.15 show the results after applying CNOT (proton control) and CNOT (carbon control) gates without uncertainty in electron Zeeman energy respectively. The results simulated with 14MHz Hamiltonian distributions can be found in appendixC.

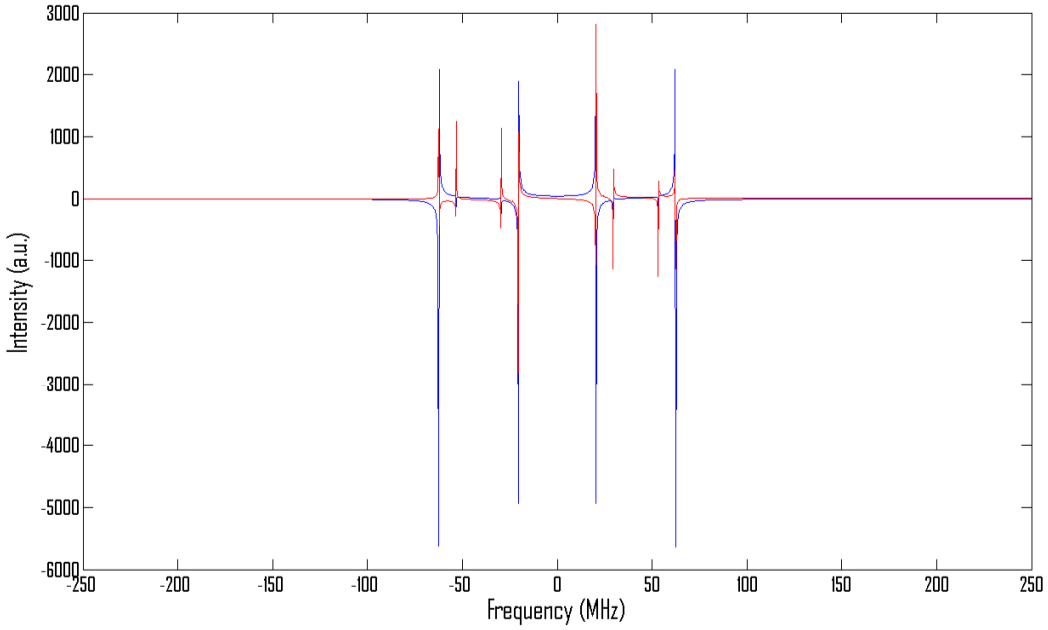

Figure 4.7: Simulated spectrum due to FID after a $\pi/2$ readout pulse after applying π GRAPE pulse without Hamiltonian distribution with $T_2 = 2.7\mu s$. Blue is the real component of the spectrum, red is the imaginary.

4.2.1 Discussion of the simulations

The simulations show that with precise pulsefinding, high fidelity control can in principle be demonstrated in this system (i.e. with $T_2 = \infty$, typical fidelity is 99%). However, due to short T_2 compared to operation time, the fidelities in real experiments are capped at 70%. Since the operation time is fixed, it is important to extend the coherence time of the electron by cooling the sample to lower temperature (i.e liquid Helium temperature).

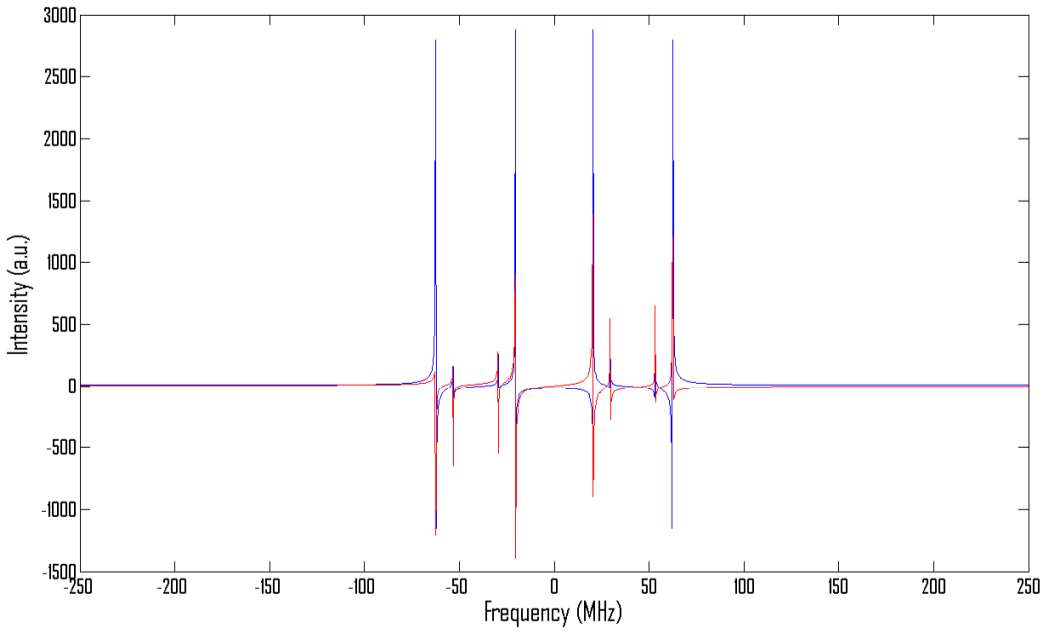

Figure 4.8: Simulated spectrum due to FID after a $\pi/2$ readout pulse without Hamiltonian distribution with $T_2 = \infty$. Blue is the real component of the spectrum, red is the imaginary. The peak intensities are different from the ones in figure4.7 due to decoherence during the pulse sequence.

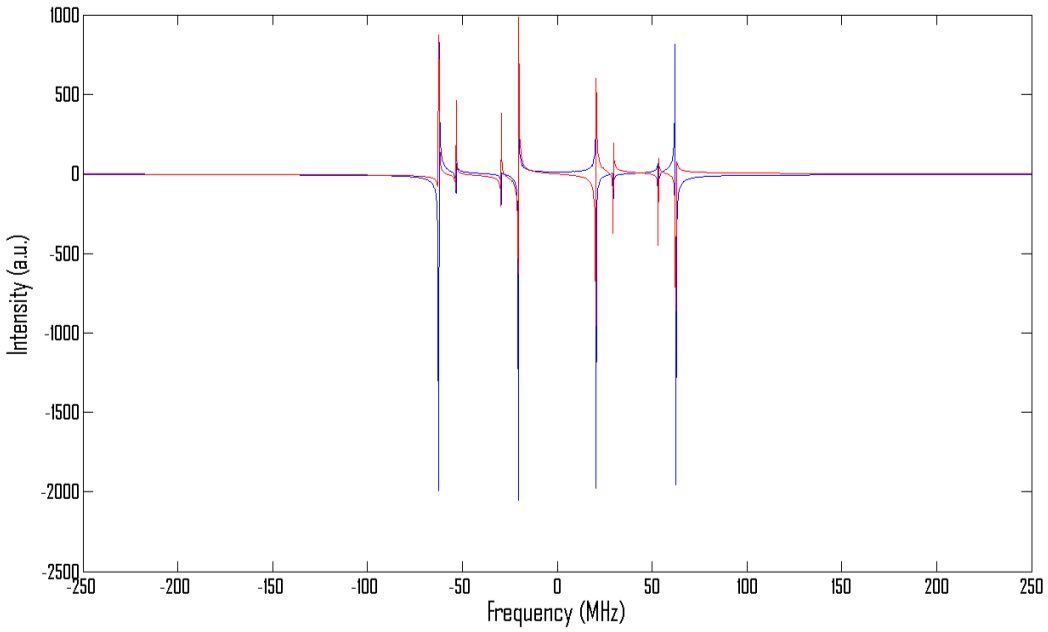

Figure 4.9: Simulated spectrum due to FID after a $\pi/2$ readout pulse after applying π GRAPE pulse without Hamiltonian distribution with $T_2 = \infty$. The state correlation between the ideal and the measured (through simulation) is 99.4%. Blue is the real component of the spectrum, red is the imaginary.

peak number		reference	with GRAPE π pulse	difference
1	phase	-91.0	88.6	179.6
	intensity	5.59e4	3.03e4	-45.8%
2	phase	-105.4	73.9	179.3
	intensity	4.23e4	2.59e4	-38.8%
3	phase	-74.6	102.8	177.4
	intensity	4.23e4	2.37e4	-44.0%
4	phase	-89.0	92.3	181.3
	intensity	5.59e4	3.15e4	-43.6%

Table 4.2: Comparison between simulated spectra (with Hamiltonian distribution with $T_2 = 2.7\mu s$) taken with readout pulse only and with GRAPE π pulse, phase in degrees and intensity in a.u.

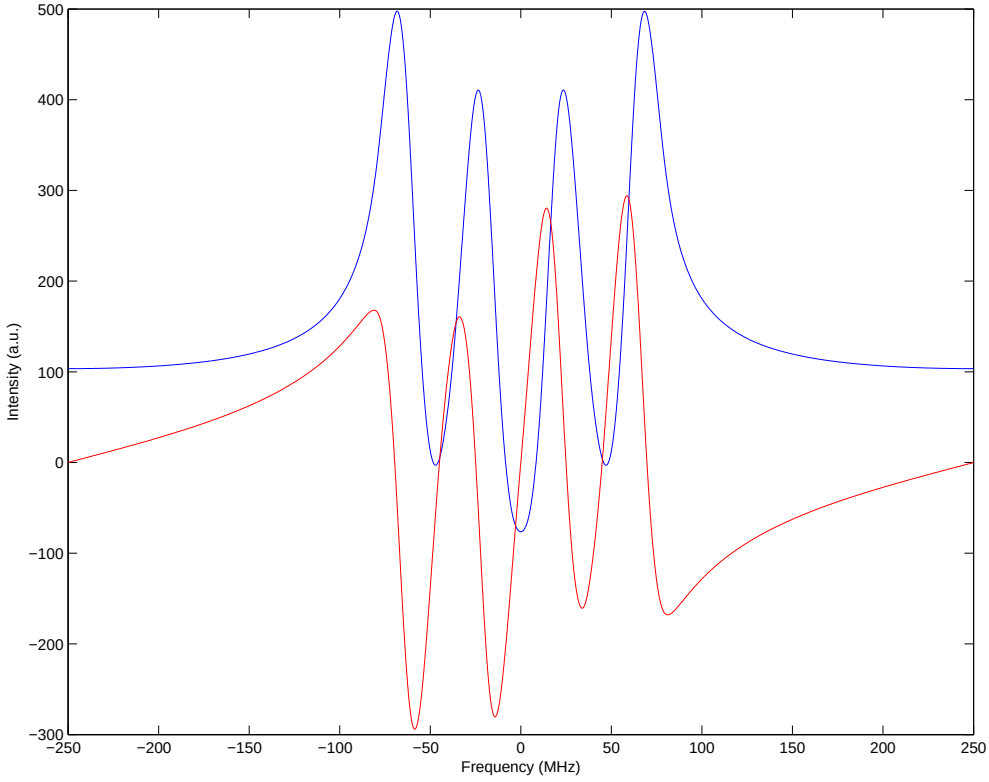

Figure 4.10: Simulated spectrum due to FID after a $\pi/2$ readout pulse with 14MHz Hamiltonian distribution with $T_2 = 2.7\mu s$. Blue is the real component of the spectrum, red is the imaginary. Note that the four peaks are not all in phase. This is because the Fourier transform does not start exactly at the beginning of the FID since the smallest time step size is 1ns in simulations.

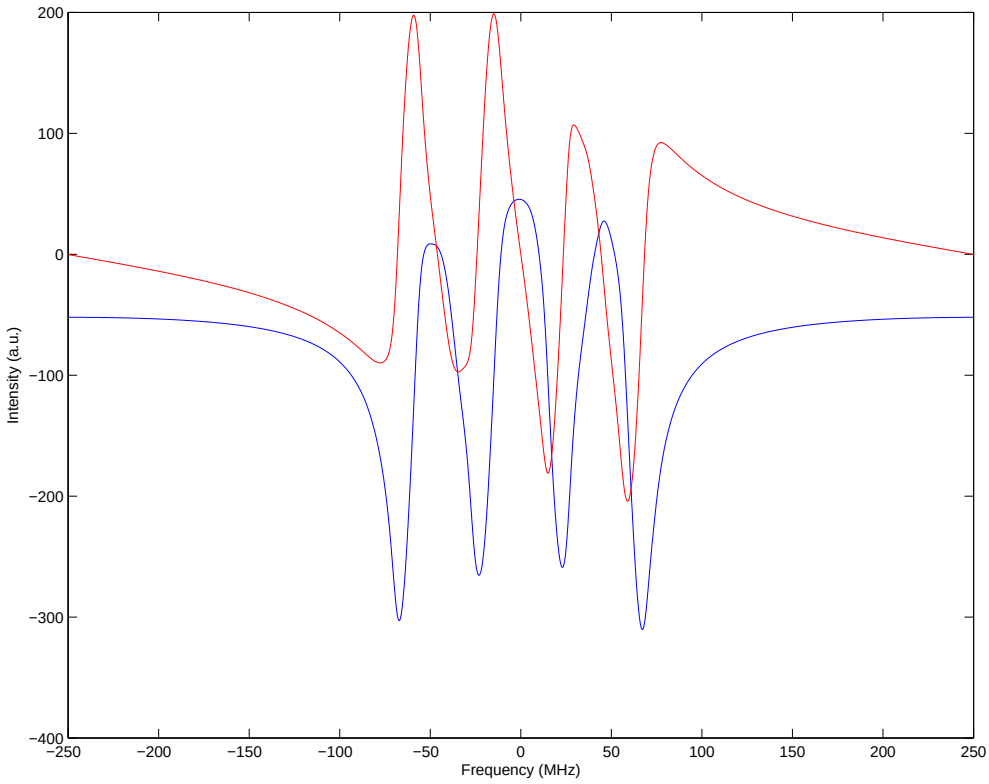

Figure 4.11: Spectrum of the system after applying π GRAPE pulse with 14MHz Hamiltonian distribution with $T_2 = 2.7\mu s$. Blue is the real component of the spectrum, red is the imaginary. The fidelity of the pulse is 60%. T_2 process contributes to the fidelity loss greatly. Another factor is that the GRAPE pulse designed is only robust again roughly 10MHz uncertainly in Zeeman energy while the actual uncertainty is 14MHz. This also results in narrower linewidth of peaks. Note that it is difficult to observe the narrowed linewidth in this plot due to the line broadening applied.

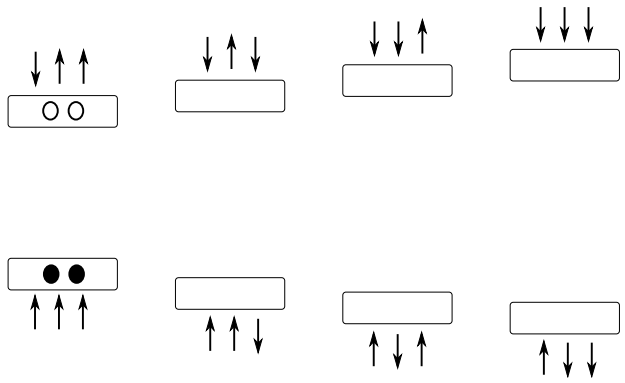

Figure 4.12: Spin population in the pseudo-pure state indicated by the number of balls.

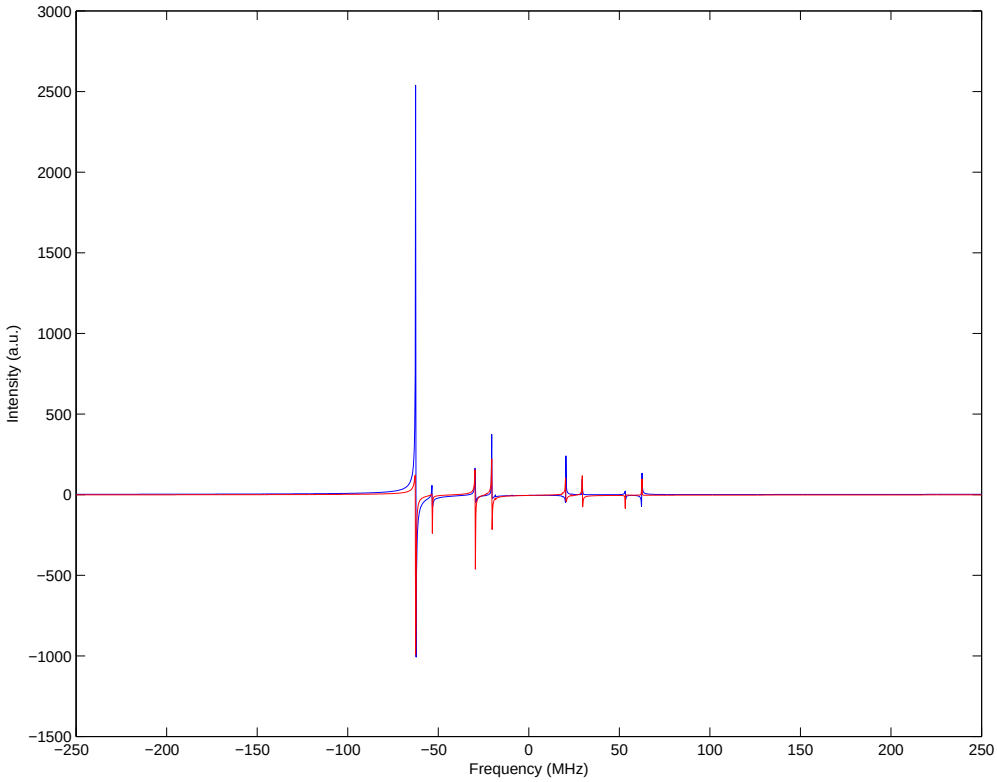

Figure 4.13: Simulated spectrum of the pseudo-pure state without Hamiltonian distribution with $T_2 = 2.7\mu s$. The state correlation of the pseudo-pure state is 90%. Note the small peaks still exist because the system is strongly coupled. Even though the population difference only present on one transition, the strong hyperfine coupling makes it possible for the electron spins to go to any other state, which results in the additional small peaks.

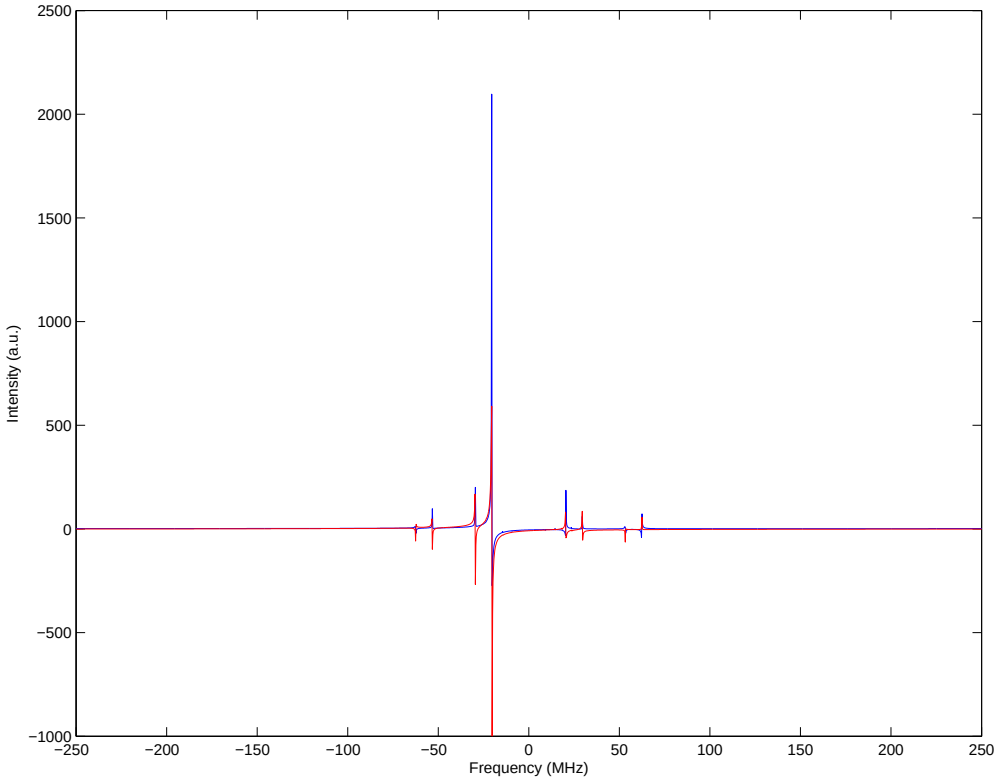

Figure 4.14: Simulated spectrum after applying CNOT (proton control) GRAPE pulse (in figure 4.4) without Hamiltonian distribution with $T_2 = 2.7\mu s$. The fidelity of the pulse is 73%.

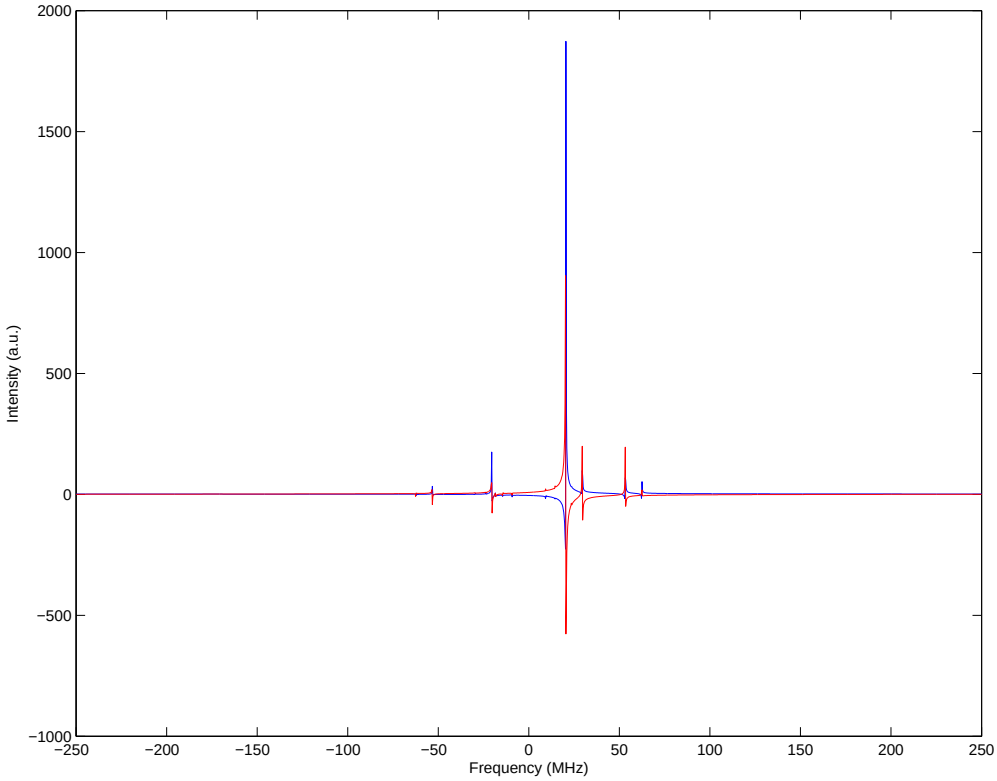

Figure 4.15: Simulated spectrum after applying CNOT (carbon control) GRAPE pulse (in figure 4.5) without Hamiltonian distribution with $T_2 = 2.7\mu s$. The fidelity of the pulse is 73%.

Chapter 5

Conclusion

The customized ESR spectrometer provides the important arbitrary pulsing ability for optimal control using GRAPE pulses. The home-built low temperature probe allows ESR experiments to be performed at liquid cryogen temperatures, enables sample re-orientation in situ and supplies a sufficient bandwidth to carry out the experiments.

The GRAPE pulses for the experiments have been designed and simulations suggest that high fidelity can be achieved in experiments with longer coherence time (lower sample temperature). The ability to implement high-fidelity control opens up many possible interesting experiments, such as implementing and testing quantum error correction codes, detailed study of decoherence process as well as error mitigation techniques such as refocusing. The experiments characterizing the fidelities of designed operations are currently underway.

Besides the current sample $\cdot CH(COOH)_2$, we are also planning to examine the $\cdot CD(COOD)_2$ system for future studies (hyperfine tensors found by Sanderud et al.[18]). The intrinsic narrower linewidth makes it easier to determine the spin Hamiltonian as well as controlling the system. The replacement of one qubit with one qutrit also means more information can be stored in the system. Last but not the least, more fundamental experiments that would make general improvements in ESR quantum computing (e.g demonstrating pulse fixing gives better fidelity and should be used for quantum computing purpose) are being considered.

APPENDICES

Appendix A

Spin polarization at finite temperature

The population of a certain spin state in equilibrium at finite temperature obeys Boltzmann distribution. The ratio of the population of spins being in the up state $n_\uparrow$ to that being in the down state $n_\downarrow$ can be written as,

$$\frac{n_\uparrow}{n_\downarrow} = exp(-\frac{E_\uparrow - E_\downarrow}{k_B T}) = exp(\frac{h\nu}{k_B T}) \tag{A.1}$$

where k_B is the Boltzmann constant, T is the temperature.

In high temperature regime (T>10K), $h\nu$ is much larger than $k_B T$. Taking Taylor expansion of the equation yields,

$$\frac{n_\uparrow}{n_\downarrow} = 1 + \frac{h\nu}{k_B T} \tag{A.2}$$

and

$$n_\uparrow = n_\downarrow + \frac{h\nu}{k_B T} n_\downarrow \tag{A.3}$$

$$n_\uparrow - n_\downarrow = \frac{h\nu}{k_B T} n_\downarrow \tag{A.4}$$

$$n_\uparrow + n_\downarrow = 2n_\downarrow + \frac{h\nu}{k_B T} n_\downarrow \tag{A.5}$$

By definition, spin polarization P is

$$P = \frac{n_\downarrow - n_\uparrow}{n_\downarrow + n_\uparrow} \tag{A.6}$$

This leads to

$$P = \frac{\frac{h\nu}{k_B T} n_\downarrow}{2n_\downarrow + \frac{h\nu}{k_B T} n_\downarrow} \tag{A.7}$$

$$\approx \frac{\frac{h\nu}{k_B T} n_\downarrow}{2n_\downarrow} \tag{A.8}$$

$$= \frac{h\nu}{2k_B T} \tag{A.9}$$

Now, the spin polarization only depends on the Larmor frequency at a fixed temperature.

The Larmor frequency depends linearly on the gyromagnetic ratio γ of the particle,

$$\nu = \frac{\gamma}{2\pi} B \tag{A.10}$$

Since the gyromagnetic ratio of the electron is 660 times larger than the proton spin, the spin polarization for electron is correspondingly larger.

Appendix B

Hyperfine tensor versus rotation angles

The electron-proton and electron-carbon hyperfine tensors are listed in equation 3.3 and 3.4 respectively. Any re-orientation of the sample can be described by three successive rotations:

1. Rotate the sample by α about the y axis (coordinates system defined in figure 3.5).

$$R_y(\alpha, 0, 0) = \begin{pmatrix} \cos(\alpha) & 0 & -\sin(\alpha) \\ 0 & 1 & 0 \\ \sin(\alpha) & 0 & \cos(\alpha) \end{pmatrix} \tag{B.1}$$

2. Rotate the sample by β about the new z axis

$$R_{z'}(0, \beta, 0) = \begin{pmatrix} \cos(\beta) & \sin(\beta) & 0 \\ -\sin(\beta) & \cos(\beta) & 0 \\ 0 & 0 & 1 \end{pmatrix} \tag{B.2}$$

3. Rotate the sample by γ about the new y axis

$$R_{y''}(0, 0, \gamma) = \begin{pmatrix} \cos(\gamma) & 0 & -\sin(\gamma) \\ 0 & 1 & 0 \\ \sin(\gamma) & 0 & \cos(\gamma) \end{pmatrix} \tag{B.3}$$

The final hyperfine tensor $\tilde{T}$ is related to the initial hyperfine tensor T by:

$$\tilde{T} = R_{y''} R_{z'} R_y T R'_y R'_{z'} R'_{y''} \tag{B.4}$$

The isotropic hyperfine term A of the tensor is $\tilde{T}(3,3)$ [(3,3) means the matrix element on row 3 and column 3] and the anisotropic hyperfine term B is $\sqrt{\tilde{T}(3,1)^2 + \tilde{T}(3,2)^2}$.

Appendix C

Spectra of CNOT gates simulations

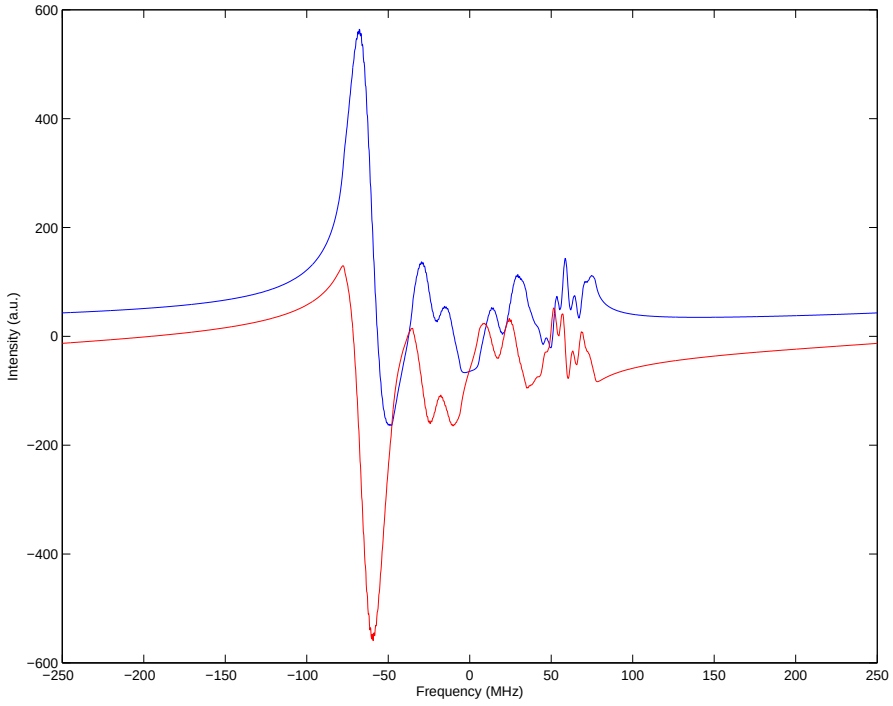

Figure C.1: Simulated spectrum of the pseudo-pure state with 14MHz Hamiltonian distribution

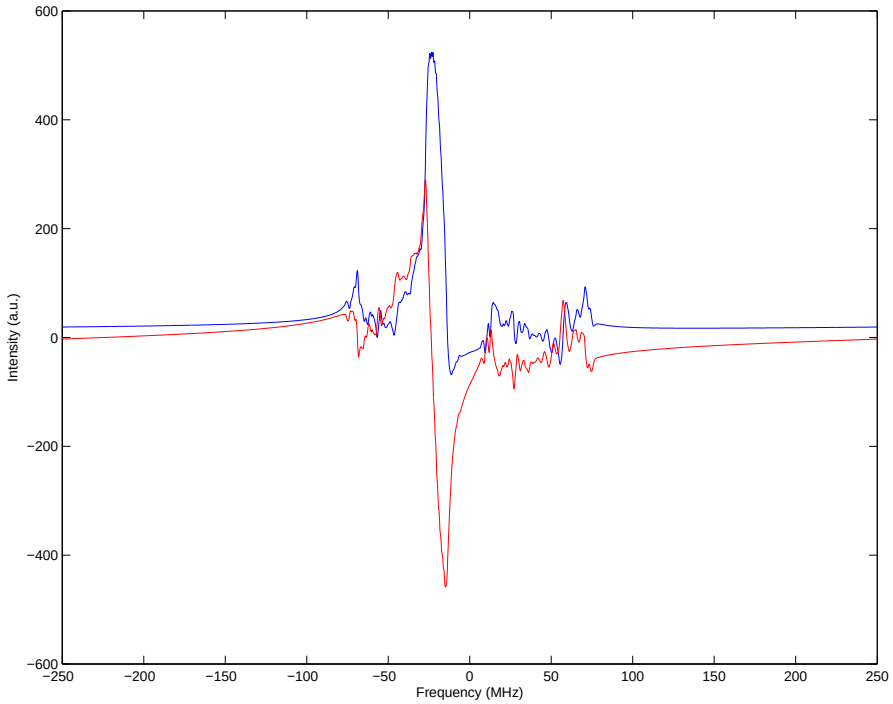

Figure C.2: Simulated spectrum after applying CNOT (proton control) GRAPE pulse (in figure 4.4) with 14MHz Hamiltonian distribution

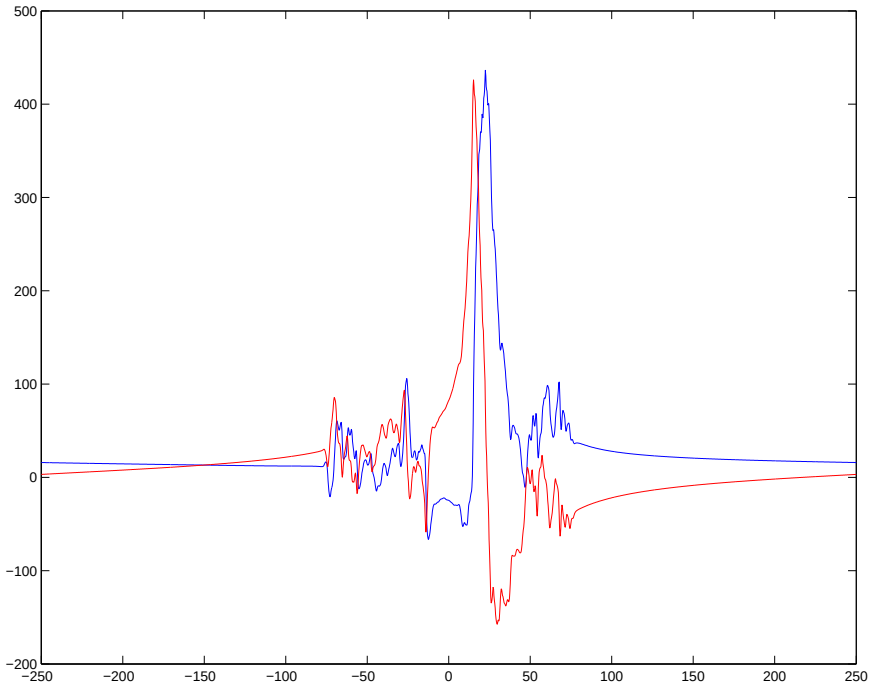

Figure C.3: Simulated spectrum after applying CNOT (carbon control) GRAPE pulse (in figure 4.5) with 14MHz Hamiltonian distribution

Bibliography

[1] J. Baugh, O. Moussa, C. A. Ryan, A. Nayak, and R. La amme. Experimental implementation of heat-bath algorithmic cooling using solid-state nuclear magnetic resonance. *nature*, 438:470–473, 2005. 18

[2] R. Bergene and T. B. Melø. Free radicals in malonic acid: a study of radical conformations 77k and 295k by the esr-technique. *Biophysik*, 9:1–12, 1972. 18

[3] I. L. Chuang, L. M. K. Vandersypen, X. Zhou, D. W. Leung, and S. Lloyd. Experimental realization of a quantum algorithm. *Nature*, 393:143–146, 1998. 2

[4] T. Cole and C. Heller. Hyperfine splitting in the (HOOC)C13H(COOH) radical. *j. chem. phys.*, 34:1085, 1961. ix, 17, 22, 23

[5] D. P. DiVincenzo. The physical implementation of quantum computation. *Fortsch. Phys.*, 48:771–793, 2000. 1

[6] Jiangfeng Du, Xing Rong, Nan Zhao, Ya Wang, Jiahui Yang, and R. B. Liu. Preserving electron spin coherence in solids by optimal dynamical decoupling. *Nature*, 461:1265–1268, 2009. 19

[7] J. Baugh et al. Quantum information processing using nuclear and electron magnetic resonance: review and prospects. *Physics in Canada - quantum information and quantum computating edition*, 63:4, 2007. 2

[8] N. Khaneja et al. Optimal control of coupled spin dynamics: design of nmr pulse sequences by gradient ascent algorithms. *j. magn. reson.*, 172:296–305, 2005. 4

[9] J. A. Goedkoop and C. H. MacGillavry. The crystal structure of malonic acid. *acta cryst.*, 10:125, 1956. 18

[10] Walter Gordy. *Theory and applications of electron spin resonance*. Wiley, New York :, 1980. 20

[11] J. S. Hodges, J. C. Yang, C. Ramanathan, and D. G. Cory. Universal control of nuclear spins via anisotropic hyperfine interactions. *Phys. Rev. A*, 78(1):010303, 2008. 4

[12] J. A. Jones, M. Mosca, and R. H. Hansen. Implementation of a quantum search algorithm on a quantum computer. *Nature*, 393:344–346, 1998. 2

[13] M. Levitt. *Spin dynamics*. Wiley, West Sussex, England, 2001. 2, 19

[14] H. M. McConnell, C. Heller, T. Cole, and R. W. Fessenden. Radiation damage in organic crystals. I: $CH(COOH)_2$ in malonic acid. *j. amer. chem. soc.*, 82:766–775, 1960. 18, 19

[15] Osama Moussa. On heat-bath algorithmic cooling and its implementation in solid-state nmr. Master's thesis, University of Waterloo, 2005. 18

[16] M. A. Nielsen and I. L. Chuang. *Quantum Computation and Quantum Information.* Cambridge University Press, Cambridge, UK, 2000. 1

[17] G. A. Rinard, R. W. Quine, S. S. Eaton, and G. R. Eaton. Microwave coupling structures for spectroscopy. *Journal of Magnetic Resonance*, 105:137–144, 1993. 8

[18] A. Sanderud, E. Sagstuen, Y. Itagaki, and A. Lund. Epr and endor studies of deuterium hyperfine and quadrupole coupling in $^{\cdot}CD(COOD)_2$: experimental and theoretical estimates of electric field gradients from an α-carbon. *j. phys. chem.*, 104:6372–6379, 2000. 20, 43

[19] A. Schweiger and G. Jeschke. *Principles of pulse electron paramagnetic resonance.* Oxford university press, New York, 2001. 3, 24

[20] P. W. Shor. Polynomial-time algorithms for prime factorization and discrete logarithms on a quantum computer. *SIAM Journal on Computing*, 26(5):1484–1509, 1997. 1